

# Consolidated theoretical/empirical predictive method for subcooled flow boiling in annuli with reference to thermal management of ultra-fast electric vehicle charging cables



V.S. Devahdhanush<sup>a</sup>, Seunghyun Lee<sup>a,b</sup>, Issam Mudawar<sup>a,\*</sup>

<sup>a</sup> Boiling and Two-Phase Flow Laboratory (PU-BTPFL), School of Mechanical Engineering, Purdue University, 585 Purdue Mall, West Lafayette, IN 47907, USA

<sup>b</sup> Gwangju Institute of Science and Technology Two-Phase Flow and Thermal Engineering Laboratory, School of Mechanical Engineering, 123 Cheomdangwagi-ro, Buk-gu, Gwangju 61005, South Korea

## ARTICLE INFO

### Article history:

Received 22 December 2020

Revised 2 March 2021

Accepted 14 March 2021

Available online 12 May 2021

### Keywords:

subcooled flow boiling  
annulus  
electric vehicles  
charging system  
thermal management  
design recommendations

## ABSTRACT

Ability to deliver very high electrical current through a charging cable is key to successful proliferation of electric vehicles (EVs). Associated with high current delivery is a host of thermal problems stemming from the need to remove enormous amounts of heat from the cable. This study seeks to develop a highly effective thermal management scheme based on subcooled flow boiling principles. The main objective is to develop a consolidated theoretical/empirical method for predicting the heat transfer and pressure drop characteristics of both laminar and turbulent flows through concentric circular annuli with uniformly heated inner wall and adiabatic outer wall. Although maintaining subcooled boiling along the entire cable is a key practical objective, this consolidated method is shown to be capable of tackling multiple flow regimes (single-phase liquid, subcooling boiling, saturated boiling, and single-phase vapor) and highly effective at predicting local surface and fluid temperatures. This method is then adopted to design and optimization of very high current EV charging cable cooling system using dielectric fluid HFE-7100 as coolant. Effects of various parameters, including electrical current, both wire and conduit sizes, inlet fluid temperature, and flow rate are carefully addressed and recommendations made for effective and robust overall system design.

© 2021 Elsevier Ltd. All rights reserved.

## 1. Introduction

### 1.1. Subcooled Flow Boiling Thermal Management of Ultra-Fast Electric Vehicle Charging Systems

Recent years have witnessed the worldwide proliferation of Electric Vehicles (EVs) for a variety of benefits they offer over conventional petroleum-oil-based vehicles (also called Internal Combustion Engine Vehicles; ICEVs) [1,2] such as (i) negligible emission and reduced overall air pollution [3–5], (ii) lower cost of operation [6], (iii) reduced noise levels [7], (iv) uncertainties in both the availability and cost of petroleum oil in the future [1,8], and finally (v) rapidly falling prices due to both government policies

and increased research and development. But there are numerous hurdles that need to be overcome to attract more people towards EVs, a major one being the average time required to charge an EV. Presently, this is much longer than the re-fueling time for petroleum-based vehicles.

Electric vehicle charging systems can be broadly classified into two based on the type of current that is conducted into the EV: Alternating Current (AC) or Direct Current (DC). Note that the electrical grid's AC needs to be converted to DC to be stored in the battery. EV chargers can also be classified into three based on their power levels: Level 1 (Opportunity), Level 2 (Primary), and Level 3 (Fast) [9–11]. Typically, DC chargers offer the fastest rates of charging, and have fewer components onboard the EV, reducing both volume and weight [12]. Numerous standards are available worldwide to ensure their uniformity and safety, the most popular being J1772, ChAdeMO, GB/T, Mennekes, and Tesla [13]. The key components of a typical DC EV charging system is illustrated

\* Corresponding author.

E-mail address: [mudawar@ecn.purdue.edu](mailto:mudawar@ecn.purdue.edu) (I. Mudawar).

URL: <https://engineering.purdue.edu/BTPFL> (I. Mudawar)

## Nomenclature

$A$	area
$A_c$	cross-sectional area
$Bo$	boiling number, $Bo = q''_s/Gh_{fg}$
$C$	empirical coefficient
$Co$	convection number
$c_p$	specific heat at constant pressure
$D$	diameter
$D_h$	hydraulic diameter
$D_{hp}$	heated perimeter diameter
$D_l$	laminar equivalent diameter
$E$	enhancement factor
$F$	empirical constant
$f$	friction factor
$Fr$	Froude number
$G$	mass velocity
$g$	gravitational acceleration
$h$	enthalpy; heat transfer coefficient
$\bar{h}$	average heat transfer coefficient
$h_{fg}$	latent heat of vaporization
$I_{\text{wire}}$	current through charging wire
$Ja^*$	modified Jakob number, $Ja^* = c_{pf}\Delta T_{\text{sub,in}}/h_{fg}$
$Ja^{**}$	modified Jakob number, $Ja^{**} = c_{pf}\Delta T_{\text{sub}}/h_{fg}$
$K$	incremental pressure drop number
$k$	thermal conductivity
$L$	length
$L^+$	non-dimensional length, $L^+ = L/(D_h \text{Re}_{sp})$
$L^*$	non-dimensional length, $L^* = L/(D_h \text{Re}_{sp} \text{Pr})$
$M_W$	molecular weight
$N$	number of segments
$Nu$	Nusselt number
$P$	pressure
$P_F$	friction perimeter
$P_H$	heated perimeter
$P_R$	reduced pressure
$Pr$	Prandtl number
$Q_v$	volumetric flow rate
$q''$	heat flux
$r^*$	radius ratio, $r^* = D_i/D_o$
$Re$	Reynolds number
$S$	safety factor; suppression factor
$T$	temperature
$\bar{T}$	average temperature
$\Delta T_{\text{sub}}$	fluid subcooling, $\Delta T_{\text{sub}} = T_{\text{sat}} - T_f$
$U$	bulk fluid velocity
$v$	specific volume
$v_{fg}$	specific volume difference between vapor and liquid
$x_e$	thermodynamic equilibrium quality
$X_{tt}$	turbulent-turbulent Lockhart-Martinelli parameter
$z$	axial coordinate

### Greek symbols

$\alpha$	void fraction; temperature coefficient of material
$\delta^+$	dimensionless hydrodynamic boundary layer thickness
$\mu$	dynamic viscosity
$\nu$	kinematic viscosity
$\omega$	parameter in mixture viscosity model
$\rho$	density; electrical resistivity of material
$\sigma$	surface tension; area ratio
$\tau_F$	frictional shear stress

### Subscripts

$ad$	adiabatic
$app$	apparent
$c$	contraction
$ch$	channel
$crit$	critical
$e$	expansion
$exp$	experimental
$f$	liquid; bulk fluid
$fd$	fully developed
$fo$	liquid only
$g$	vapor
$h$	heated
$hy$	hydrodynamic entrance
$i$	inner tube of annulus
$in$	channel inlet
$k$	index for a phase: liquid ( $f$ ) or vapor ( $g$ )
$l$	based on $D_l$
$max$	maximum
$nb$	nucleate boiling
$o$	outer tube of annulus
$out$	channel outlet
$p$	plenum
$pred$	predicted
$s$	surface
$sat$	saturation
$sb$	saturated boiling
$sc$	subcooled boiling
$sp$	single-phase
$th$	thermal entrance
$tot$	total
$tp$	two-phase
$z$	local (along axial direction)

### Acronyms

AC	Alternating Current
AWG	American Wire Gauge
CHF	Critical Heat Flux
DC	Direct Current
EV	Electric Vehicle
HEM	Homogeneous Equilibrium Model
ICEV	Internal Combustion Engine Vehicle
MAE	Mean Absolute Error (%)
ONB	Onset of Nucleate Boiling
SFM	Separated Flow Model

in Fig. 1, where the combined charging system type 1 standard (J1772 + CCS) connector is shown as an example.

Decreasing EV charging times means the transfer of larger amounts of energy in shorter durations and can be accomplished by either increasing the charging current or voltage, or both. Increasing the charging voltage is accompanied by safety and cybersecurity risks as well as various other limiting factors discussed in [14]. Increasing the charging current is a potentially better path to developing ultra-fast EV chargers. The main obstacle to this method is the large amount of heat dissipated in the conducting elements, particularly charging cables and connectors. This study is concerned entirely with developing a thermal management scheme to dissipate heat from the charging cable of high-current ultra-fast EV chargers.

A review of EV chargers available in market today revealed that almost all low-power EV chargers utilize natural air convection to dissipate the small amounts of heat generated. And higher-current charging cables are cooled by forced air and liquid convection. The charging rate of the fastest commercially available charger is ~500 kW, with the highest continuous current of charging cables be-

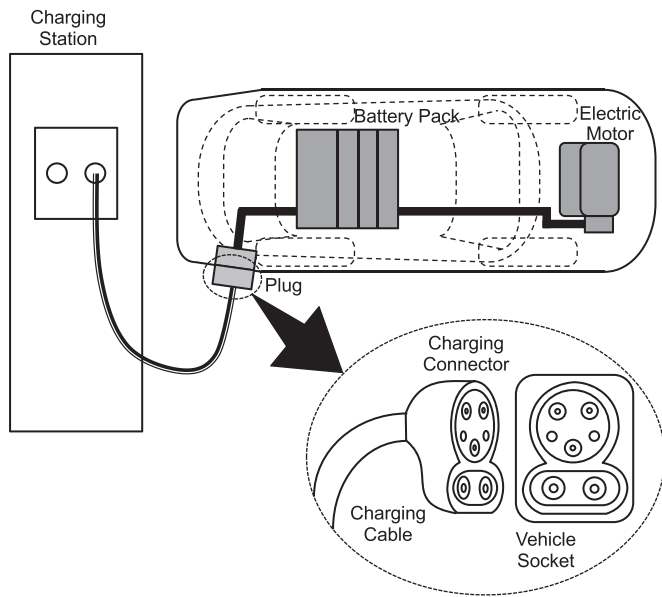


**Fig. 1.** Key components of a typical DC electric vehicle charging system. Combined Charging System Type 1 standard (J1772 AC + CCS) connector is shown as an example.

ing ~500 A. Literature suggests that, including all losses, the effective gasoline refueling (energy transfer) rate of a light passenger ICEV is ~5000 kW [15,16]. On comparing both, it is clear that today's fastest EV charging occurs at a rate one order of magnitude lower than ICEV refueling time. Further increases in charging current would lead to substantial amounts of heat dissipation within the cables, and even single-phase liquid cooling can no longer be used to cool them.

As opposed to single-phase, two-phase cooling schemes capitalize on both the coolant's sensible heat (associated with an increase in coolant's temperature) and latent heat (resulting from phase change from liquid to vapor) to greatly enhance heat dissipation rates [17]. Researchers at both the Purdue University Boiling and Two-Phase Flow Laboratory (PU-BTPFL) and other labs around the world have studied and developed various boiling configurations including pool boiling, channel flow boiling, jet impingement, sprays, and combinations thereof. In this study, subcooled flow boiling is proposed as a thermal management scheme that could cater to cooling high-current charging cables of ultra-fast EV chargers.

Most subcooled flow boiling studies are focused on conventional channel shapes [18,19], with a smaller subset focused on flow in annuli [19–24]. With two heat transfer walls, annuli flow can have more combinations of boundary conditions and are classified into four kinds: either uniform heat flux or temperature of inner tube, and either uniform temperature or adiabatic outer tube [25,26]. Single-phase solutions to all other boundary conditions could easily be found from the above four kinds by simple interpolation techniques.

For a more detailed introduction on EV chargers and subcooled flow boiling, the reader is directed to the authors' companion study [27].

## 1.2. Recap of the Authors' Experimental Investigation

The present study builds on the knowledge gained from the authors' companion experimental study [27], so a brief recap of the same is provided to benefit the reader.

The study [27] focused on experimental investigation of subcooled flow boiling in annuli. Based on a preliminary analysis, an

experimental facility was built with a test module similar to a section of charging cable and cooling conduit assembly. A custom-built heater was used to mimic heat generation due to high current supply through 6.35-mm diameter charging wire carrying continuous currents ranging from 726 to 2438 A. Highly subcooled dielectric liquid HFE-7100 was pumped through a 304.8-mm long heated section of a horizontal concentric circular annulus of uniformly heated inner surface (heater) and adiabatic outer tube (conduit) of respective diameters 6.35 mm and 23.62 mm. Various test cases of different operating conditions were conducted to experimentally illustrate the performance of the cooling system and explain the heat transfer physics within the test module. The 820 collected datapoints were demarcated into their respective flow regimes using flow regime contour maps. Careful assessment of prior subcooled boiling correlations showed best predictions are realized using the Moles and Shaw [28] correlation, evidenced by a MAE of 11.68%.

Overall, it was experimentally shown that this thermal management scheme could be utilized to cool down cables carrying up to 2438 A continuous current, which is roughly four times higher than today's fastest commercial EV chargers.

But experimentation is not always the most viable option in most cases. Alternate methods of prediction and estimation of results are usually sought after by both design engineers and researchers.

## 1.3. Predictive Methods for Flow Boiling Heat Transfer

The high costs, long times, and large tedious efforts of experimentation has led both design engineers and researchers to seek alternate methods that help predict important parameters and arrive at results in an expeditious, inexpensive, and user-friendly manner. Such predictive methods yield a plethora of information that help in the thermal management system design and optimization process. Some of the various predictive methods available for two-phase flow and heat transfer include empirical and semi-empirical methods, and, to a lesser extent, theoretical and computational models, with each having their own advantages and disadvantages.

Owing to the complexity of two-phase flow and heat transfer, empirical and semi-empirical correlations remain the most widely used approaches of prediction. They are typically directly derived from experimental data and are simple to use. But a key disadvantage is most having been developed using relatively small databases and are applicable to very narrow ranges of operating conditions and geometrical parameters, though some investigators [29–31] have rectified this by amassing large databases from the world literature to develop their own correlations. Another disadvantage of correlations is that, while they may enable prediction of certain parameters for which they were specifically developed (such as heat transfer coefficient and pressure drop), they are incapable of predicting intricate flow features.

Theoretical models are preferred for most flow situations as they are universally applicable once validated for wide ranges of experimental parameters. But presently, theoretical models are available only for very specific flow situations such as annular flow in circular and rectangular channels or growth and lift-off of a single bubble. Given this major limitation, they are not popular as design tools. For example, given the different flow regimes along the flow direction of subcooled flow boiling in annuli, theoretical models are simply not available for each individual regime.

Computational fluid dynamics (CFD) tools constitute another prediction approach and have been gaining popularity in the design of thermal systems [32,33]. They yield the most detailed results, including temporal and spatial flow fields, which is not possible with other prediction methods and even experiments. Although

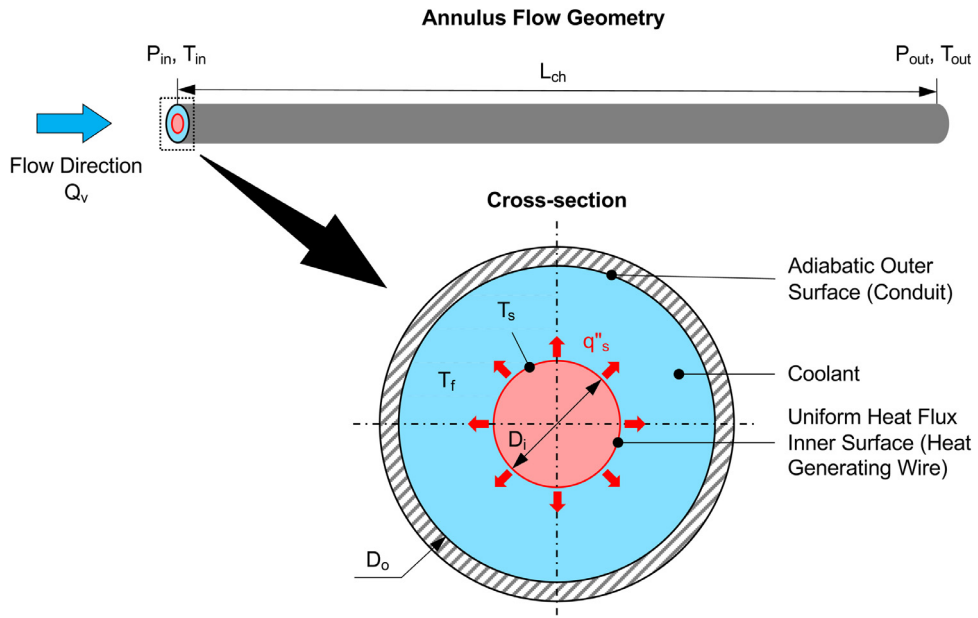


**Fig. 2.** Schematics of annulus flow geometry and boundary conditions.

this method has shown great success in simulating single-phase flows, two-phase flow simulation still faces many challenges, including the need for more powerful and expensive computational resources, and inaccuracies of the sub-models used. For example, even with the availability of such resources, results from a single case may still require several weeks for convergence [33]. And a simple go-to CFD approach is not yet available, and the various sub-models need to be carefully chosen based on validation with experimental conditions.

It is possible to develop a consolidated theoretical/empirical method that is based on several individual models and correlations developed by theoretical, semi-empirical, or empirical means. By taking advantage of the high prediction accuracy of each model or correlation for various physical parameters in different regions of the flow, the consolidated method constitutes the best available approach to predicting relevant parameters throughout the flow domain. Such a method was previously proposed by Kim and Mudawar [34] to predict subcooled and saturated flow boiling in micro-channel heat sinks, and later adapted by Devahdhanush *et al.* [33] for subcooled flow boiling in both micro- and macro-channel heat sinks.

#### 1.4. Objectives of Study

The main objective of this study is to develop a robust method to predict subcooled flow boiling in concentric circular annuli with uniformly heated inner tube and adiabatic outer tube. The consolidated theoretical/empirical method is derived from the experimental conclusions of [27]. A key advantage of this method is its ability to tackle both laminar and turbulent flows through annuli, including single-phase liquid convection, subcooled flow boiling, saturated flow boiling, and single-phase vapor convection. This method is compared with subcooled flow boiling experimental data for validation against a broad range of Reynolds numbers.

This method is adopted to the EV charger thermal management application by replacing the inner heated tube with a heat generating charging wire, and predictions are made for a typical 5.00-m long wire to demonstrate the effects of various parameters on system performance. Finally, key recommendations are made to aid in system design and optimization.

## 2. Consolidated Theoretical/Empirical Method

### 2.1. Overview of the Method

**Fig. 2** depicts the annulus flow geometry, system nomenclature, and boundary conditions. The flow domain of length  $L_{ch}$  is divided into  $N$  small discrete segments of equal length,  $\Delta z$  ( $N = 1000$  in this study). Steady-state calculations for different physical parameters are performed in each segment in a coupled fashion, wherein pressure drop and heat transfer calculations are performed simultaneously. Both cross-sectional variations and gravitational effects are assumed to be negligible. **Table 1** lists all the input parameters required, resulting output parameters, operating conditions, and constraints imposed when using this method. The consolidated method has the capability of tackling all possible flow regimes from single-phase liquid to subcooled boiling to saturated boiling to even single-phase vapor in both the laminar and turbulent flow regimes. The single-phase liquid flow regime is further subdivided into simultaneously (hydrodynamically and thermally) developing, thermally developing, and fully developed. The thermal boundary layer cannot become developed before the development of hydrodynamic boundary layer because of the dependence of heat transfer on convective effects of the liquid [35]. Also, since the liquid Prandtl number for most coolants and operating temperatures of interest is above unity, momentum diffusivity dominates over thermal diffusivity and renders the hydrodynamic boundary layer fully developed before the thermal boundary layer [26]. It is emphasized that not all flow regimes would be present in all cases, and the contributions of each regime are rather dictated by the operating conditions and geometrical parameters.

**Tables 2** and **3** list all respective theoretical and empirical relations used in the consolidated predictive method for determining pressure drop and heat transfer in the concentric annulus. Although both laminar and turbulent flow regimes are shown on the left and right sides of the tables, respectively, it is noted that flow rates in most practical applications are found to fall into the turbulent regime. The critical Reynolds number,  $Re_{f,crit}$ , at which transition from laminar to turbulent flow occurs is dependent on the radius ratio,  $r^*$ . The lower limit of  $Re_{f,crit}$  has been given in graphical form by Hanks [36], with values of 2100 and 2285 at the re-

**Table 1**

Key information on consolidated theoretical/empirical method.

Input parameters	Fluid (for thermophysical properties) Mass flow rate (or volume flow rate) Charging current (or surface heat flux) Inner (wire/conductor) diameter Outer (conduit) diameter Length of conduit Inlet temperature Inlet saturation temperature (or inlet pressure)
Important output parameters	Pressure drop Heat transfer coefficient Inner (wire) surface temperature Fluid temperature Heat generation rate Thermodynamic equilibrium quality
Operating modes	Single-phase forced convection Subcooled flow boiling Saturated flow boiling
Constraints	Avoid sub-atmospheric Avoid choked flow

spective extremes of  $r^* = 0$  and 1, and maximum value of 2462 at  $r^* = 0.15$ . For simplicity, a constant value of  $\text{Re}_{f,crit} \cong 2400$  is used in this study.

## 2.2. Pressure Drop

The total pressure drop,  $\Delta P_{tot}$ , includes the drop due to geometrical contraction at the inlet,  $\Delta P_c$ , single-phase region,  $\Delta P_{sp}$ , two-phase region,  $\Delta P_{tp}$ , and recovery due to geometrical expansion at the outlet,  $\Delta P_e$ . The single-phase pressure drop is further composed of two components: upstream liquid pressure drop,  $\Delta P_{sp,f}$ , and downstream vapor pressure drop,  $\Delta P_{sp,g}$ . And the two-phase pressure drop is composed of two components: subcooled boiling,  $\Delta P_{sc}$ , and saturated boiling,  $\Delta P_{sb}$ .

### 2.2.1. Contraction Pressure Loss

The contraction pressure drop is given by Collier and Thome's [37] relation, where  $\sigma_c$  is the contraction area ratio and  $C_c$  a contraction coefficient associated with the formation of venae contracta. For single-phase flows, Geiger [38] defined  $C_c$  as a function of  $\sigma_c$ , and for two-phase flows at the inlet, the effect of venae contracta is neglected and  $C_c = 1$  based on the recommendations of Schmidt and Friedel [39] and Abdelall *et al.* [40].

### 2.2.2. Single-phase Liquid Flow Regime

**Laminar Flows** – The hydrodynamic entrance length for laminar flows is given by Liu's [41] results, based on the recommendation of Shah and London [42]. The apparent friction factor in the hydro-dynamically developing region is given by the derivation of Shah [43] and is dependent on parameters  $K(\infty)$ ,  $f, \text{Re}$ , and  $C$ , whose values are available in tabulated form. Here,  $K$  is the incremental pressure drop number, a measure of the pressure drop contribution due to momentum change and increased wall shear as the flow becomes fully developed;  $K$  increases from 0 at the inlet towards a constant value  $K(\infty)$  in the fully developed region.  $f, \text{Re}$  is for fully developed flow and approaches 16 for  $r^* = 0$  (an infinitesimal inner tube or a regular tube flow) and 24 for  $r^* = 1$  (flat duct flow).  $C$  is a constant purely based on the tube geometry [43]. In all regions downstream of the hydrodynamic entrance length, the velocity profile becomes constant at all locations and the boundary layer fully developed. The friction factor for this region is given by a popular analytical relation from [25,42]. The right side of this relation becomes 16 when  $r^* = 0$ , the expression for circular tube flow.

**Turbulent Flows** – There are not as many studies in the literature addressing turbulent single-phase flows in annuli as compared to laminar flows. As proposed by Jones and Leung [44], a

laminar equivalent diameter,  $D_l$ , for concentric annuli is calculated and used in place of the hydraulic diameter,  $D_h$ , in turbulent circular tube flow equations. This approach has been shown to reduce errors in prediction of fully developed flow friction factor in annuli [44,45]. The hydrodynamic entrance length for turbulent flows has been much debated in the literature for circular tube flows, with multiple relations yielding different predictions [45,46]. This is because of the dependence of  $L_{hy}$  on numerous hard-to-control parameters like inlet turbulence intensity, wall surface roughness, and minor disturbances [46]. Bhatti and Shah [45] showed that, for a Reynolds number of 38,800, the predictions of 7 different relations from the literature lie in the range of  $L_{hy}/D_h = 15.6 - 41.6$ . For concentric annuli, one of the first acceptable relations was given by Olson and Sparrow [47] based on their experimental results for two annulus geometries as  $20 < L_{hy}/D_h < 25$ , independent of  $r^*$ . A recent study by Shome [48] yielded relations for  $L_{hy}$  and the hydrodynamically developing friction factor as functions of  $r^*$  based on results from a Reynolds Averaged Navier-Stokes (RANS) numerical model results using the  $k-\omega$  turbulence model. Although the RANS model was validated against Direct Numerical Simulation (DNS) results, there is no validation against experimental results by other investigators, and as such this model is not recommended at present. The relation by Zhi-qing [49] has been recommended by researchers because of its ease of use and validation against experimental studies [26,45]. Zhi-qing's relation for circular tubes is extended to concentric annular flow by replacing  $D_h$  with  $D_l$  and the resulting equations for  $L_{hy}$  and friction factor are used. Friction factor for the fully developed regime is determined from the Blasius and McAdams relations in the lower ( $\text{Re}_l \leq 20,000$ ) and higher ( $\text{Re}_l > 20,000$ ) turbulence ranges, respectively, both using  $D_l$ .

### 2.2.3. Subcooled Flow Boiling Regime

The criteria for Onset of Nucleate Boiling (ONB) is discussed in detail in [27]. Sato and Matsumura's [50] relation is used to predict the surface temperature at ONB,  $T_{s,ONB}$ , and the most upstream location at which the local surface temperature exceeds  $T_{s,ONB}$  marks the onset of boiling.

The ratio of subcooled flow boiling pressure drop to single-phase adiabatic pressure drop is given by Hahne *et al.* [51] for refrigerants in circular tubes and annuli. This relation inherently incorporates the effects of annulus geometry, system pressure, and fluid thermophysical properties.

### 2.2.4. Saturated Flow Boiling Regime

Saturated flow boiling is initiated after thermodynamic equilibrium quality,  $x_e$ , reaches zero value. Pressure drop in this regime

**Table 2**

Consolidated theoretical/empirical method for determining pressure drop for two-phase flow along an annulus.

Total pressure drop																																						
$\Delta P_{tot} = \Delta P_c + \Delta P_{sp} + \Delta P_{qp} + \Delta P_e; \Delta P_{sp} = \Delta P_{sp,f} + \Delta P_{sp,g}; \Delta P_{qp} = \Delta P_{sc} + \Delta P_{sb}; \Delta P_{sp,k} = \frac{2f_{app} G^2 L_{sp,k} v_k}{D_h}$																																						
Contraction pressure loss																																						
$\Delta P_c = \frac{G^2 v_f}{2} \left[ \left( \frac{1}{C_c} - 1 \right)^2 + (1 - \sigma_c^2) \right] \left[ 1 + \frac{v_{fg} X_{e,in}}{v_f} \right] [37]; \sigma_c = \frac{A_{ch}}{A_{p,in}}$																																						
$C_c = 1 - \frac{1 - \sigma_c}{2.08(1 - \sigma_c) + 0.5371}$ for single-phase inlet [38]; $C_c = 1$ for two-phase inlet [39,40]																																						
Hydrodynamic entrance length																																						
Laminar [41,42]	Turbulent																																					
<table border="1"> <tr> <td><math>r^*</math></td><td>0</td><td>0.05</td><td>0.10</td><td>0.50</td><td>0.75</td><td>1.0</td><td></td></tr> <tr> <td><math>L_{hy}</math></td><td>0.0541</td><td>0.0206</td><td>0.0175</td><td>0.0116</td><td>0.0109</td><td>0.0108</td><td></td></tr> </table> $L^+ = \frac{L}{Re_{sp} D_h}$	$r^*$	0	0.05	0.10	0.50	0.75	1.0		$L_{hy}$	0.0541	0.0206	0.0175	0.0116	0.0109	0.0108		$L_{hy} = 1.3590 Re_i^{1/4} D_l$ [49] $Re_i = GD_l / \mu_f$ $D_l = D_h \frac{1 + r^{*2} + (1 - r^{*2}) / \ln r^*}{(1 - r^*)^2}$ [44]																					
$r^*$	0	0.05	0.10	0.50	0.75	1.0																																
$L_{hy}$	0.0541	0.0206	0.0175	0.0116	0.0109	0.0108																																
Single-phase hydrodynamically developing flow ( $L < L_{hy}$ )																																						
Laminar [43]	Turbulent [49]																																					
$f_{app} Re_{sp} = \frac{3.44}{\left(L^+\right)^{0.5}} + \frac{K(\infty)/\left(4L^+\right) + f Re - 3.44/\left(L^+\right)^{0.5}}{1 + C_{hy} \left(L^+\right)^{-2}}$ <table border="1"> <tr> <td><math>r^*</math></td><td>0</td><td>0.05</td><td>0.10</td><td>0.50</td><td>0.75</td><td>1.0</td><td></td></tr> <tr> <td><math>K(\infty)</math></td><td>1.250</td><td>0.830</td><td>0.784</td><td>0.688</td><td>0.678</td><td>0.674</td><td></td></tr> <tr> <td><math>f Re</math></td><td>16.000</td><td>21.567</td><td>22.343</td><td>23.813</td><td>23.967</td><td>24.000</td><td></td></tr> <tr> <td><math>C</math></td><td>0.0002 12</td><td>0.0000 50</td><td>0.0000 43</td><td>0.0000 32</td><td>0.0000 30</td><td>0.0000 29</td><td></td></tr> </table>	$r^*$	0	0.05	0.10	0.50	0.75	1.0		$K(\infty)$	1.250	0.830	0.784	0.688	0.678	0.674		$f Re$	16.000	21.567	22.343	23.813	23.967	24.000		$C$	0.0002 12	0.0000 50	0.0000 43	0.0000 32	0.0000 30	0.0000 29		$L_{sp}/D_l = 1.4039 Re_i^{0.25} \delta^{+1.25} \left( \begin{array}{l} 1 + 0.1577 \delta^+ - 0.1793 \delta^{+2} \dots \\ -0.0168 \delta^{+3} + 0.0064 \delta^{+4} \end{array} \right)$ when $\delta^+ < 1$ (developing region), $f_{app} = \left[ \frac{1}{\left(1 - 0.25 \delta^+ + 0.0667 \delta^{+2}\right)^2} - 1 \right] \frac{0.25}{L_{sp}/D_l}$ when $\delta^+ = 1$ (developed region),					
$r^*$	0	0.05	0.10	0.50	0.75	1.0																																
$K(\infty)$	1.250	0.830	0.784	0.688	0.678	0.674																																
$f Re$	16.000	21.567	22.343	23.813	23.967	24.000																																
$C$	0.0002 12	0.0000 50	0.0000 43	0.0000 32	0.0000 30	0.0000 29																																
							$f_{app} = \left[ 0.07 + 0.316 \frac{L_{sp}/D_l}{Re_i^{0.25}} \right] \frac{0.25}{L_{sp}/D_l}$																															
Single-phase fully developed flow ( $L \geq L_{hy}$ )																																						
Laminar [25,42]	Turbulent [45]																																					
$f_{app} Re_{sp} = \frac{16(1 - r^*)^2}{1 + r^{*2} - 2r_{max}^{*2}}; r_{max}^* = \left( \frac{1 - r^{*2}}{2 \ln(1/r^*)} \right)^{1/2}$	$f = 0.0791 Re_i^{-0.25}$ for $2400 \leq Re_i \leq 20,000$ (Blasius) $f = 0.046 Re_i^{-0.2}$ for $Re_i > 20,000$ (McAdams)																																					
Onset of nucleate boiling																																						
$T_s > T_{s,ONB} = T_{sat} + \frac{4\sigma T_{sat} v_{fg} h}{k_f h_{fg}} \left( 1 + \sqrt{1 + \frac{k_f h_{fg}}{2\sigma T_{sat} v_{fg} h} (T_{sat} - T_f)} \right)$ [50]																																						
Subcooled flow boiling																																						
$\frac{\Delta P_{sc}}{\Delta P_{ad}} = 1 + 500 Bo^{1.6} Ja^{*-1.2} \left( \frac{v_g}{v_f} \cdot \frac{P_H}{P_F} \right)$ [51]; $Bo = \frac{q''_s}{Gh_{fg}}$ ; $Ja^* = \frac{c_{p,f} \Delta T_{sub,in}}{h_{fg}}$																																						
Saturated flow boiling																																						
Homogeneous Equilibrium Model (HEM)																																						
Two-phase mixture density, $\frac{1}{\bar{\rho}} = \frac{1}{x_e v_g + (1 - x_e) v_f} = x_e v_g + (1 - x_e) v_f = \bar{v}$ ; Void fraction, $\alpha = \left[ 1 + \left( \frac{\rho_g}{\rho_f} \right) \left( \frac{1 - x_e}{x_e} \right) \right]^{-1}$ $- \left( \frac{dP}{dz} \right) = \frac{\left\{ 1 + \frac{G^2 v_{fg}}{h_{fg}} [x_e v_g + (1 - x_e) v_f] \right\} \left\{ \frac{1}{2} G^2 f_p [x_e v_g + (1 - x_e) v_f] \right\} \frac{P_f}{A_c} + G^2 v_{fg} \left( \frac{q''_s P_H}{GA_c h_{fg}} \right)}$ $\tau_F = \frac{1}{2} \frac{G^2}{\bar{\rho}} f_p = \frac{1}{2} G^2 f_p [x_e v_g + (1 - x_e) v_f]; Re_{sp} = \frac{GD_h}{\mu_{sp}}$																																						
Two-phase mixture viscosity, $\mu_{sp} = \omega \mu_g + (1 - \omega)(1 + 2.5\omega) \mu_f; \omega = \frac{x_e v_g}{v_f + x_e v_g}$ [52]																																						
$f_{sp} = 16 Re_{sp}^{-1}$ for $Re_{sp} < 2400$							$f_{sp} = 0.079 Re_{sp}^{-0.25}$ for $2400 \leq Re_{sp} < 20,000$ $f_{sp} = 0.046 Re_{sp}^{-0.2}$ for $Re_{sp} \geq 20,000$																															
Single-phase vapor flow																																						
Same relations as single-phase liquid fully developed flow, but with thermophysical properties of pure vapor																																						
Expansion pressure recovery																																						
$\Delta P_c = G^2 \sigma_e (\sigma_e - 1) v_f \left[ 1 + \frac{v_{fg} X_{e,out}}{v_f} \right]$ [37]; $\sigma_e = \frac{A_{ch}}{A_{p,out}}$																																						

can be predicted using either the Homogeneous Equilibrium Model (HEM) or the Separated Flow Model (SFM). HEM treats the two-phase fluid mixture as a pseudo single-phase fluid with averaged properties that obey simple single-phase conservation equations. Assumed are uniform pressure across the flow area, and both uniform and equal velocities of the two phases. SFM, using the 'slip flow' formulation, considers the two-phase fluid to be artificially separated into liquid and vapor phases, with each phase having its

own uniform velocity. As opposed to SFM, HEM is derived without the use of empirically determined constants and can therefore be used to model flow in annuli with greater confidence. However, HEM needs the determination of two-phase friction factor,  $f_{tp}$ , which can be either a constant or calculated using the mixture viscosity method. The mixture viscosity model of Beattie and Whalley [52] has been shown to give best overall predictions in all laminar liquid-laminar vapor, laminar liquid-turbulent vapor,

**Table 3**

Consolidated theoretical/empirical method for determining heat transfer for two-phase flow along an annulus.

Thermal entrance length, $L_{th}$																																																																																																																																																		
<b>Laminar</b> [42] $L_{th} = (D_h \text{Re} \Pr) L_{th}^*$																																																																																																																																																		
<table border="1"> <thead> <tr> <th><math>r^*</math></th><th>0.02</th><th>0.05</th><th>0.10</th><th>0.25</th><th>0.50</th><th>1.00</th></tr> </thead> <tbody> <tr> <td><math>L_{th}^*</math></td><td>0.02699</td><td>0.03043</td><td>0.03334</td><td>0.03726</td><td>0.03975</td><td>0.04101</td></tr> </tbody> </table>							$r^*$	0.02	0.05	0.10	0.25	0.50	1.00	$L_{th}^*$	0.02699	0.03043	0.03334	0.03726	0.03975	0.04101																																																																																																																														
$r^*$	0.02	0.05	0.10	0.25	0.50	1.00																																																																																																																																												
$L_{th}^*$	0.02699	0.03043	0.03334	0.03726	0.03975	0.04101																																																																																																																																												
<b>Turbulent</b> [49,61,63] $L_{th} \approx 1.3590 \text{Re}^{1/4} D_t + 4D_l$																																																																																																																																																		
Single-phase simultaneously developing flow ( $L < L_{hy}$ )																																																																																																																																																		
<b>Laminar</b> [55,56]																																																																																																																																																		
<table border="1"> <thead> <tr> <th><math>r^*</math></th><th colspan="6">Nu</th></tr> <tr> <th><math>L^*</math></th><th><math>Pr = 0.01</math></th><th><math>Pr = 0.7</math></th><th><math>Pr = 10</math></th><th></th><th></th><th></th></tr> <tr> <th></th><th>0.25</th><th>0.50</th><th>0.25</th><th>0.50</th><th>0.25</th><th>0.50</th></tr> </thead> <tbody> <tr> <td>0.00025</td><td>50.77</td><td>49.5</td><td>40.56</td><td>35.52</td><td>30.24</td><td>27.546</td></tr> <tr> <td>0.0005</td><td>37.8</td><td>36.52</td><td>27.87</td><td>25.9</td><td>23.64</td><td>21.106</td></tr> <tr> <td>0.001</td><td>28.19</td><td>26.93</td><td>21.16</td><td>19.24</td><td>18.92</td><td>16.54</td></tr> <tr> <td>0.0025</td><td>19.265</td><td>18.02</td><td>15.22</td><td>13.395</td><td>14.53</td><td>12.4</td></tr> <tr> <td>0.005</td><td>14.64</td><td>13.39</td><td>12.47</td><td>10.5</td><td>12.085</td><td>10.14</td></tr> <tr> <td>0.01</td><td>11.39</td><td>10.13</td><td>10.19</td><td>8.5</td><td>10.226</td><td>8.44</td></tr> <tr> <td>0.025</td><td>8.787</td><td>7.497</td><td>8.546</td><td>6.924</td><td>8.572</td><td>6.934</td></tr> <tr> <td>0.05</td><td>7.922</td><td>6.497</td><td>7.931</td><td>6.351</td><td>7.934</td><td>6.353</td></tr> <tr> <td>0.1</td><td>7.758</td><td>6.171</td><td>7.759</td><td>6.19</td><td>7.759</td><td>6.19</td></tr> <tr> <td>100</td><td>7.753</td><td>6.181</td><td>7.735</td><td>6.181</td><td>7.753</td><td>6.181</td></tr> </tbody> </table>							$r^*$	Nu						$L^*$	$Pr = 0.01$	$Pr = 0.7$	$Pr = 10$					0.25	0.50	0.25	0.50	0.25	0.50	0.00025	50.77	49.5	40.56	35.52	30.24	27.546	0.0005	37.8	36.52	27.87	25.9	23.64	21.106	0.001	28.19	26.93	21.16	19.24	18.92	16.54	0.0025	19.265	18.02	15.22	13.395	14.53	12.4	0.005	14.64	13.39	12.47	10.5	12.085	10.14	0.01	11.39	10.13	10.19	8.5	10.226	8.44	0.025	8.787	7.497	8.546	6.924	8.572	6.934	0.05	7.922	6.497	7.931	6.351	7.934	6.353	0.1	7.758	6.171	7.759	6.19	7.759	6.19	100	7.753	6.181	7.735	6.181	7.753	6.181																																																	
$r^*$	Nu																																																																																																																																																	
$L^*$	$Pr = 0.01$	$Pr = 0.7$	$Pr = 10$																																																																																																																																															
	0.25	0.50	0.25	0.50	0.25	0.50																																																																																																																																												
0.00025	50.77	49.5	40.56	35.52	30.24	27.546																																																																																																																																												
0.0005	37.8	36.52	27.87	25.9	23.64	21.106																																																																																																																																												
0.001	28.19	26.93	21.16	19.24	18.92	16.54																																																																																																																																												
0.0025	19.265	18.02	15.22	13.395	14.53	12.4																																																																																																																																												
0.005	14.64	13.39	12.47	10.5	12.085	10.14																																																																																																																																												
0.01	11.39	10.13	10.19	8.5	10.226	8.44																																																																																																																																												
0.025	8.787	7.497	8.546	6.924	8.572	6.934																																																																																																																																												
0.05	7.922	6.497	7.931	6.351	7.934	6.353																																																																																																																																												
0.1	7.758	6.171	7.759	6.19	7.759	6.19																																																																																																																																												
100	7.753	6.181	7.735	6.181	7.753	6.181																																																																																																																																												
Single-phase thermally developing flow ( $L_{hy} < L < L_{th}$ )																																																																																																																																																		
<b>Laminar</b> [42]																																																																																																																																																		
<table border="1"> <thead> <tr> <th><math>r^*</math></th><th colspan="6">Nu</th></tr> <tr> <th><math>L^*</math></th><th>0.02</th><th>0.05</th><th>0.1</th><th>0.25</th><th>0.5</th><th>1</th></tr> </thead> <tbody> <tr> <td>0.000025</td><td>-</td><td>-</td><td>71.556</td><td>59.307</td><td>53.969</td><td>50.740</td></tr> <tr> <td>0.00005</td><td>-</td><td>-</td><td>58.019</td><td>47.480</td><td>42.960</td><td>40.257</td></tr> <tr> <td>0.0001</td><td>86.900</td><td>58.000</td><td>47.265</td><td>38.099</td><td>34.233</td><td>31.95</td></tr> <tr> <td>0.00025</td><td>70.400</td><td>45.500</td><td>36.356</td><td>28.615</td><td>25.418</td><td>23.567</td></tr> <tr> <td>0.0005</td><td>61.200</td><td>38.600</td><td>30.027</td><td>23.153</td><td>20.351</td><td>18.754</td></tr> <tr> <td>0.001</td><td>54.010</td><td>33.170</td><td>24.960</td><td>18.838</td><td>16.356</td><td>14.965</td></tr> <tr> <td>0.0025</td><td>46.480</td><td>27.580</td><td>20.000</td><td>14.515</td><td>12.367</td><td>11.193</td></tr> <tr> <td>0.005</td><td>41.850</td><td>24.200</td><td>17.120</td><td>12.075</td><td>10.127</td><td>9.081</td></tr> <tr> <td>0.01</td><td>38.093</td><td>21.521</td><td>14.903</td><td>10.219</td><td>8.433</td><td>7.490</td></tr> <tr> <td>0.015</td><td>36.319</td><td>20.278</td><td>13.889</td><td>9.381</td><td>7.668</td><td>6.773</td></tr> <tr> <td>0.025</td><td>34.556</td><td>19.060</td><td>12.904</td><td>8.573</td><td>6.931</td><td>6.086</td></tr> <tr> <td>0.05</td><td>33.126</td><td>18.091</td><td>12.128</td><td>7.938</td><td>6.353</td><td>5.546</td></tr> <tr> <td>0.1</td><td>32.729</td><td>17.827</td><td>11.918</td><td>7.764</td><td>6.192</td><td>5.395</td></tr> <tr> <td>0.15</td><td>32.706</td><td>17.812</td><td>11.907</td><td>7.754</td><td>6.182</td><td>5.385</td></tr> <tr> <td>0.25</td><td>32.705</td><td>17.811</td><td>11.906</td><td>7.753</td><td>6.181</td><td>5.385</td></tr> <tr> <td>0.5</td><td>32.705</td><td>17.811</td><td>11.906</td><td>7.753</td><td>6.181</td><td>5.385</td></tr> <tr> <td>1</td><td>32.705</td><td>17.811</td><td>11.906</td><td>7.753</td><td>6.181</td><td>5.385</td></tr> <tr> <td>100</td><td>32.705</td><td>17.811</td><td>11.906</td><td>7.753</td><td>6.181</td><td>5.385</td></tr> </tbody> </table>							$r^*$	Nu						$L^*$	0.02	0.05	0.1	0.25	0.5	1	0.000025	-	-	71.556	59.307	53.969	50.740	0.00005	-	-	58.019	47.480	42.960	40.257	0.0001	86.900	58.000	47.265	38.099	34.233	31.95	0.00025	70.400	45.500	36.356	28.615	25.418	23.567	0.0005	61.200	38.600	30.027	23.153	20.351	18.754	0.001	54.010	33.170	24.960	18.838	16.356	14.965	0.0025	46.480	27.580	20.000	14.515	12.367	11.193	0.005	41.850	24.200	17.120	12.075	10.127	9.081	0.01	38.093	21.521	14.903	10.219	8.433	7.490	0.015	36.319	20.278	13.889	9.381	7.668	6.773	0.025	34.556	19.060	12.904	8.573	6.931	6.086	0.05	33.126	18.091	12.128	7.938	6.353	5.546	0.1	32.729	17.827	11.918	7.764	6.192	5.395	0.15	32.706	17.812	11.907	7.754	6.182	5.385	0.25	32.705	17.811	11.906	7.753	6.181	5.385	0.5	32.705	17.811	11.906	7.753	6.181	5.385	1	32.705	17.811	11.906	7.753	6.181	5.385	100	32.705	17.811	11.906	7.753	6.181	5.385
$r^*$	Nu																																																																																																																																																	
$L^*$	0.02	0.05	0.1	0.25	0.5	1																																																																																																																																												
0.000025	-	-	71.556	59.307	53.969	50.740																																																																																																																																												
0.00005	-	-	58.019	47.480	42.960	40.257																																																																																																																																												
0.0001	86.900	58.000	47.265	38.099	34.233	31.95																																																																																																																																												
0.00025	70.400	45.500	36.356	28.615	25.418	23.567																																																																																																																																												
0.0005	61.200	38.600	30.027	23.153	20.351	18.754																																																																																																																																												
0.001	54.010	33.170	24.960	18.838	16.356	14.965																																																																																																																																												
0.0025	46.480	27.580	20.000	14.515	12.367	11.193																																																																																																																																												
0.005	41.850	24.200	17.120	12.075	10.127	9.081																																																																																																																																												
0.01	38.093	21.521	14.903	10.219	8.433	7.490																																																																																																																																												
0.015	36.319	20.278	13.889	9.381	7.668	6.773																																																																																																																																												
0.025	34.556	19.060	12.904	8.573	6.931	6.086																																																																																																																																												
0.05	33.126	18.091	12.128	7.938	6.353	5.546																																																																																																																																												
0.1	32.729	17.827	11.918	7.764	6.192	5.395																																																																																																																																												
0.15	32.706	17.812	11.907	7.754	6.182	5.385																																																																																																																																												
0.25	32.705	17.811	11.906	7.753	6.181	5.385																																																																																																																																												
0.5	32.705	17.811	11.906	7.753	6.181	5.385																																																																																																																																												
1	32.705	17.811	11.906	7.753	6.181	5.385																																																																																																																																												
100	32.705	17.811	11.906	7.753	6.181	5.385																																																																																																																																												
Single-phase fully developed flow ( $L > L_{th}$ )																																																																																																																																																		
<b>Laminar</b> [26,42]																																																																																																																																																		
<table border="1"> <thead> <tr> <th><math>r^*</math></th><th colspan="6">Nu</th></tr> </thead> <tbody> <tr> <td>0.01</td><td>54.01669</td><td></td><td></td><td></td><td></td><td></td></tr> <tr> <td>0.02</td><td>32.70512</td><td></td><td></td><td></td><td></td><td></td></tr> <tr> <td>0.04</td><td>20.50925</td><td></td><td></td><td></td><td></td><td></td></tr> <tr> <td>0.05</td><td>17.81128</td><td></td><td></td><td></td><td></td><td></td></tr> <tr> <td>0.08</td><td>13.46806</td><td></td><td></td><td></td><td></td><td></td></tr> <tr> <td>0.10</td><td>11.90578</td><td></td><td></td><td></td><td></td><td></td></tr> <tr> <td>0.15</td><td>9.68703</td><td></td><td></td><td></td><td></td><td></td></tr> <tr> <td>0.25</td><td>7.75347</td><td></td><td></td><td></td><td></td><td></td></tr> <tr> <td>0.40</td><td>6.58330</td><td></td><td></td><td></td><td></td><td></td></tr> <tr> <td>0.50</td><td>6.18102</td><td></td><td></td><td></td><td></td><td></td></tr> <tr> <td>0.80</td><td>5.57849</td><td></td><td></td><td></td><td></td><td></td></tr> <tr> <td>1.0</td><td>5.38462</td><td></td><td></td><td></td><td></td><td></td></tr> </tbody> </table>							$r^*$	Nu						0.01	54.01669						0.02	32.70512						0.04	20.50925						0.05	17.81128						0.08	13.46806						0.10	11.90578						0.15	9.68703						0.25	7.75347						0.40	6.58330						0.50	6.18102						0.80	5.57849						1.0	5.38462																																																						
$r^*$	Nu																																																																																																																																																	
0.01	54.01669																																																																																																																																																	
0.02	32.70512																																																																																																																																																	
0.04	20.50925																																																																																																																																																	
0.05	17.81128																																																																																																																																																	
0.08	13.46806																																																																																																																																																	
0.10	11.90578																																																																																																																																																	
0.15	9.68703																																																																																																																																																	
0.25	7.75347																																																																																																																																																	
0.40	6.58330																																																																																																																																																	
0.50	6.18102																																																																																																																																																	
0.80	5.57849																																																																																																																																																	
1.0	5.38462																																																																																																																																																	
<b>Turbulent</b> [65]																																																																																																																																																		
<table border="1"> <thead> <tr> <th><math>Re</math></th><th colspan="5">Nu (<math>r^* = 0.10</math>)</th></tr> <tr> <th><math>Pr</math></th><th>10000</th><th>30000</th><th>100000</th><th>300000</th><th>1000000</th></tr> </thead> <tbody> <tr> <td>0</td><td>11.5</td><td>11.5</td><td>11.5</td><td>11.5</td><td>11.6</td></tr> <tr> <td>0.001</td><td>11.5</td><td>11.5</td><td>11.5</td><td>11.7</td><td>12.3</td></tr> <tr> <td>0.003</td><td>11.5</td><td>11.5</td><td>11.7</td><td>12.6</td><td>17.0</td></tr> <tr> <td>0.01</td><td>11.8</td><td>11.8</td><td>13.5</td><td>19.4</td><td>39.0</td></tr> <tr> <td>0.03</td><td>12.5</td><td>14.1</td><td>21.8</td><td>42.0</td><td>103</td></tr> <tr> <td>0.5</td><td>40.8</td><td>81.0</td><td>191</td><td>443</td><td>1160</td></tr> <tr> <td>0.7</td><td>48.5</td><td>98.0</td><td>235</td><td>550</td><td>1510</td></tr> <tr> <td>1</td><td>58.5</td><td>120</td><td>292</td><td>700</td><td>1910</td></tr> <tr> <td>3</td><td>93.5</td><td>206</td><td>535</td><td>1300</td><td>3720</td></tr> <tr> <td>10</td><td>140</td><td>328</td><td>890</td><td>2300</td><td>6700</td></tr> </tbody> </table>							$Re$	Nu ( $r^* = 0.10$ )					$Pr$	10000	30000	100000	300000	1000000	0	11.5	11.5	11.5	11.5	11.6	0.001	11.5	11.5	11.5	11.7	12.3	0.003	11.5	11.5	11.7	12.6	17.0	0.01	11.8	11.8	13.5	19.4	39.0	0.03	12.5	14.1	21.8	42.0	103	0.5	40.8	81.0	191	443	1160	0.7	48.5	98.0	235	550	1510	1	58.5	120	292	700	1910	3	93.5	206	535	1300	3720	10	140	328	890	2300	6700																																																																				
$Re$	Nu ( $r^* = 0.10$ )																																																																																																																																																	
$Pr$	10000	30000	100000	300000	1000000																																																																																																																																													
0	11.5	11.5	11.5	11.5	11.6																																																																																																																																													
0.001	11.5	11.5	11.5	11.7	12.3																																																																																																																																													
0.003	11.5	11.5	11.7	12.6	17.0																																																																																																																																													
0.01	11.8	11.8	13.5	19.4	39.0																																																																																																																																													
0.03	12.5	14.1	21.8	42.0	103																																																																																																																																													
0.5	40.8	81.0	191	443	1160																																																																																																																																													
0.7	48.5	98.0	235	550	1510																																																																																																																																													
1	58.5	120	292	700	1910																																																																																																																																													
3	93.5	206	535	1300	3720																																																																																																																																													
10	140	328	890	2300	6700																																																																																																																																													

(continued on next page)

**Table 3** (continued)

	30	195	478	1320	3470	10300
	100	272	673	1910	5030	15200
	1000	486	1240	3600	9600	28700
<b>Nu (<math>r^* = 0.20</math>)</b>						
$Pr \backslash Re$	10000	30000	100000	300000	1000000	
0	8.40	8.30	8.30	8.30	8.30	
0.001	8.40	8.40	8.30	8.40	8.90	
0.003	8.40	8.40	8.50	9.05	12.5	
0.01	8.50	8.60	9.70	14.0	33.6	
0.03	9.00	10.1	15.8	31.7	81.0	
0.5	31.2	64.0	157	370	980	
0.7	38.6	79.8	196	473	1270	
1	46.8	99.0	247	600	1640	
3	77.4	175	465	1150	3250	
10	120	290	800	2050	6000	
30	172	428	1210	3150	9300	
100	243	617	1760	4630	13800	
1000	448	1400	3280	8800	26000	
<b>Nu (<math>r^* = 0.50</math>)</b>						
$Pr \backslash Re$	10000	30000	100000	300000	1000000	
0	6.28	6.30	6.30	6.30	6.30	
0.001	6.28	6.30	6.30	6.40	6.75	
0.003	6.28	6.30	6.40	6.85	9.40	
0.01	6.37	6.45	7.30	10.8	23.2	
0.03	6.75	7.53	12.0	24.8	35.5	
0.5	24.6	52.0	130	310	835	
0.7	30.9	66.0	166	400	1080	
1	38.2	83.5	212	520	1420	
3	66.8	152	402	1010	2870	
10	106	260	715	1850	5400	
30	153	386	1080	2850	8400	
100	220	558	1600	4250	12600	
1000	408	1040	3000	8000	24000	
<b>Nu (<math>r^* = 0.80</math>)</b>						
$Pr \backslash Re$	10000	30000	100000	300000	1000000	
0	5.87	5.90	5.92	5.95	5.97	
0.001	5.87	5.90	5.92	6.00	6.33	
0.003	5.87	5.90	6.03	6.40	8.80	
0.01	5.95	6.07	6.80	10.0	21.7	
0.03	6.20	7.05	11.4	23.0	61.0	
0.5	22.9	49.5	123	296	800	
0.7	28.5	62.3	157	384	1050	
1	35.5	78.3	202	492	1350	
3	63.0	145	386	973	2750	
10	102	248	393	1790	5150	
30	147	370	1050	2750	8100	
100	215	540	1540	4050	12100	
1000	393	1000	2890	7700	23000	
<b>Subcooled flow boiling</b>						
For $x_e \leq -0.05$ ,						
$\frac{Nu_{sc}}{Nu_{sp}} = 78.5 \left( \frac{q_s''}{h_{fg} \rho_g U} \right)^{0.67} \left( \frac{h_{fg}}{c_{p,f} \Delta T_{sub}} \right)^{0.5} \left( \frac{\rho_g}{\rho_f} \right)^{0.7} \left( \frac{c_{p,f} \mu_f}{k_f} \right)^{0.46}$						
$= 78.5 Bo^{0.67} Ja^{**-0.5} \left( \frac{\rho_g}{\rho_f} \right)^{0.03} Pr_f^{0.46}$						
For $-0.05 < x_e < 0$ , $h_{sc}$ is determined based on a linear extrapolation of $h_{sc}$ at $x_e = -0.1$ and $-0.05$ (refer to section 2.3.2 for details).						
<b>Saturated flow boiling</b>						

(continued on next page)

turbulent liquid-laminar vapor, and turbulent liquid-turbulent vapor flow regimes by Kim and Mudawar [53,54] for all two-phase flows (adiabatic, boiling, and condensation), which is why this viscosity model is also adopted in the present study. The two-phase Reynolds number,  $Re_{tp}$ , is calculated using this mixture viscosity model, and then used to calculate the two-phase friction factor,  $f_{tp}$ , using different expressions for laminar and turbulent flow regimes.

#### 2.2.5. Single-phase Vapor Flow Regime

After all liquid has been evaporated, the channel would be filled with single-phase vapor. Predictions for this flow regime can be made using the assumption of fully developed flow and the same relations given in section 2.2.2 can be used for laminar and turbulent flows, but with liquid properties replaced by those for vapor. Typically, this flow regime is not encountered in practical flow

**Table 3** (continued)

<b>Option 1:</b> Gungor and Winterton (1987) [67] (used in this study with $D_h$ unless mentioned otherwise)
$\frac{h_{sb}}{h_{sp}} = E = 1 + 3000 Bo^{0.86} + 1.12 \left( \frac{x_e}{1-x_e} \right)^{0.75} \left( \frac{\rho_f}{\rho_g} \right)^{0.41}$
For horizontal tubes with $Fr_f < 0.05$ : $E = EFr_f^{0.1+2Fr_f}$
<b>Option 2:</b> Gungor and Winterton (1986) [30]
$h_{sb} = Eh_{sp} + Sh_{nb}; h_{nb} = 55P_R^{0.12} (-\log_{10}(P_R))^{-0.55} M_w^{-0.5} q_s^{0.67}; E = 1 + 24000 Bo^{1.16} + 1.37 X_n^{-0.86}; S = (1 + 1.15 \times 10^{-6} E^2 \text{Re}_f^{1.17})^{-1}$
For horizontal tubes with $Fr_f \leq 0.05$ : $E = EFr_f^{0.1+2Fr_f}$ and $S = SFr_f^{0.5}$
$X_n = \left( \frac{\mu_f}{\mu_g} \right)^{0.1} \left( \frac{1-x_e}{x_e} \right)^{0.9} \left( \frac{v_f}{v_g} \right)^{0.5}$
<b>Option 3:</b> Shah (1982) [70]
$\frac{h_{sb}}{h_{sp}} = \begin{cases} \max \{1.8Co^{-0.8}, F \cdot Bo^{0.5} \exp(2.47Co^{-0.15})\}, & Co \leq 0.1 \\ \max \{1.8Co^{-0.8}, F \cdot Bo^{0.5} \exp(2.74Co^{-0.1})\}, & 0.1 < Co \leq 1 \\ \max \{1.8Co^{-0.8}, h_{nb}/h_{sp}\}, & Co > 1 \end{cases}$
$\frac{h_{nb}}{h_{sp}} = \begin{cases} 1 + 46Bo^{0.5}, & Bo < 0.3 \times 10^{-4} \\ 230Bo^{0.5}, & Bo > 0.3 \times 10^{-4} \end{cases}; F = \begin{cases} 15.43, & Bo < 11 \times 10^{-4} \\ 14.7, & Bo \geq 11 \times 10^{-4} \end{cases}; Co = \left( \frac{1}{x_e} - 1 \right)^{0.8} \left( \frac{\rho_g}{\rho_f} \right)^{0.5}$
For horizontal tubes with $Fr_f \leq 0.04$ : $Co$ in above equations to be replaced by $0.38Fr_f^{-0.3}Co$
<b>Option 4:</b> Liu and Winterton (1991) [31]
$h_{sb} = \left[ (Eh_{sp})^2 + (Sh_{nb})^2 \right]^{0.5}; h_{nb} = 55P_R^{0.12} (-\log_{10}(P_R))^{-0.55} M_w^{-0.5} q_s^{0.67}; E = \left[ 1 + x_e \text{Pr}_f \left( \frac{v_g}{v_f} - 1 \right) \right]^{0.35}; S = (1 + 0.055E^2 \text{Re}_{f0}^{0.16})^{-1}$
For horizontal tubes with $Fr_f \leq 0.05$ : $E = EFr_f^{0.1+2Fr_f}$ and $S = SFr_f^{0.5}$
<b>Single-phase vapor flow</b>
Same relations as single-phase liquid fully developed flow, but with thermophysical properties of pure vapor

boiling applications as Critical Heat Flux (CHF) is encountered upstream of  $x_e = 1$ .

### 2.2.6. Expansion Pressure Recovery

Fluid at the exit of the annular channel is usually collected in a plenum with a larger cross-sectional flow area. The corresponding pressure recovery is given by Collier and Thome's relation [37].

### 2.3. Heat Transfer

Heat transfer calculations are also performed for different flow regimes along the length of the channel: single-phase liquid forced convection, subcooled flow boiling, saturated flow boiling, and single-phase vapor forced convection.

#### 2.3.1. Single-phase Liquid Flow Regime

The single-phase liquid forced convection regime is composed of simultaneously developing, thermally developing, and fully developed flow regimes for both laminar and turbulent flows.

**Laminar Flows** – The thermal entrance length,  $L_{th}$ , for laminar flows is determined from Shah and London [42] as a function of radius ratio,  $r^*$ . Axial locations that are within the hydrodynamic and thermal entrance lengths form the simultaneously developing flow region ( $L^+ < L_{hy}^+, L^* < L_{th}^*$ ). Local Nusselt number for this region is dependent on axial location, radius ratio, and liquid Prandtl number, and can be calculated from the tabulations of Kakac and Yucel [55,56]. Since their results are available only for  $r^* = 0.25$  and  $0.50$ , which incidentally is the range within which most practical annuli lie, other values are obtained by linear interpolation between the two. For significantly low  $r^*$  values, the reader is directed to theoretical values from the study by Heaton *et al.* [57]. Downstream of where the velocity boundary layer becomes fully developed, flow falls in the thermally developing region ( $L^+ \geq L_{hy}^+, L^* < L_{th}^*$ ). The local  $Nu$  in this region is available from tabulated results by Shah and London [42] as a function of axial location and radius ratio.

These results are based on the augmented results of Lundberg *et al.* [25,58] and Worsøe-Schmidt [59]. The laminar fully developed region ( $L^+ \geq L_{hy}^+, L^* \geq L_{th}^*$ ) lies downstream of the location where the thermal boundary layer becomes fully developed. Local Nusselt number in this region is constant for a specific geometry and is given by Shah and London [42].

**Turbulent Flows** – There is no validated relation available to determine the thermal entrance length,  $L_{th}$ , for turbulent flows as a function of Reynolds number, Prandtl number, and  $r^*$ . Quarmby [60], Lee [61], and Lee and Park [62] showed that for concentric annuli,  $L_{th}$  with a fully developed inlet velocity profile increases with increasing  $Re$ , although this dependence weakens at higher  $Re$ . They all agree that  $L_{th}$  increases with  $r^*$  of the annulus, but all their graphical results are based on  $Pr \approx 0.7$ . Lee [61] further showed that for a fixed  $r^*$ ,  $L_{th}$  is strongly affected by both  $Pr$  and entrance length definition (1% or 5%). For higher  $Pr$  fluids in both circular tubes and annuli,  $L_{th}$  is negligibly affected by  $Re$  [61,63]. As a result, for fully developed inlet velocity profile, an approximate constant value of  $L_{th}/D_l \approx 4$  is used for simplicity based on Lee [61] and Notter and Sleicher [63]. This  $L_{th}$  is much smaller than  $L_{hy}$  for all Reynolds numbers. There is no relation available for  $L_{th}$  for cases with a uniform velocity profile (also called combined entrance length). A summation of Zhi-qing's  $L_{hy}$  and the above relation for  $L_{th}$  is suggested for obtaining an approximate  $L_{th}$  for uniform inlet velocity profile (alternatively, since the entrance length of turbulent flows is much smaller than that of laminar flows, turbulent flow may be assumed to be fully developed from the inlet for long tubes with acceptable error [35]; this approximation is not used in the present study). Again, there are no correlation equations, tabulations, or graphical results available for  $Nu$  of thermally developing flow of high  $Pr$  fluids in concentric annuli. In the thermally developing regime, Al-Arabi's [64] correlation for thermally developing flow in circular tubes is used with the fully developed  $Nu$  by Kays and Leung [65] to incorporate the effect of  $r^*$ . The same equations are used for both the simultaneously devel-

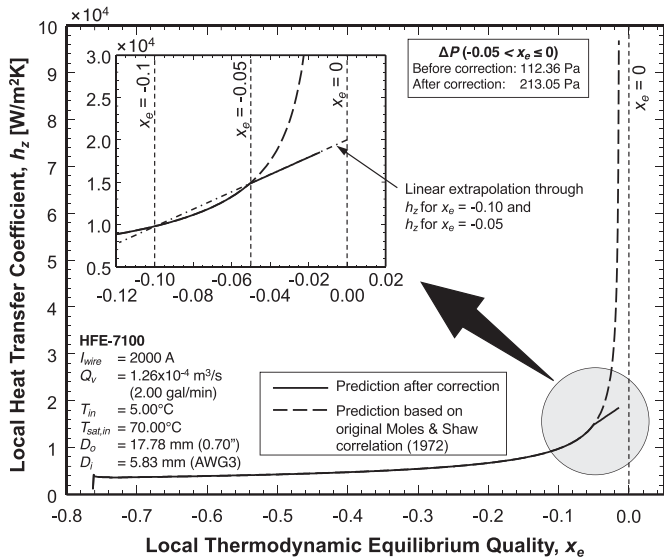


**Fig. 3.** Correction of predicted local heat transfer coefficient in the near-saturated subcooled boiling regime, shown for a set of geometrical parameters and operating conditions.

oping and thermally developing flow regions because of negligible differences in  $Nu$  between the two [66]. Finally, the local  $Nu$  in the fully developed turbulent flow region is available from tabulated results by Kays and Leung [65] as a function of  $Re$ ,  $Pr$ , and  $r^*$ .

### 2.3.2. Subcooled Flow Boiling Regime

A detailed discussion of appropriate correlations for predicting heat transfer in the subcooled boiling regime in annuli is given in the authors' companion study [27]. Moles and Shaw's [28] correlation was concluded to yield the most accurate prediction of heat transfer coefficient in this flow regime. It should be noted that this correlation performs poorly at near-saturation temperatures because the  $\Delta T_{sub}^{-0.5}$  factor would result in infinite  $Nu$  [21,28]. To avoid this singularity, this correlation is only used for  $x_e \leq -0.05$  rather than  $x_e < 0$ .  $Nu$  in the region  $-0.05 < x_e < 0$  is predicted by a linear extrapolation of the subcooled boiling predictions in the region  $-0.10 \leq x_e \leq -0.05$ ; reasons for this linear approximation is purely mathematical, is the simplest and most indicative of the slope of the  $h_z$  vs.  $x_e$  curve in this near-saturation region. This is illustrated in Fig. 3 for a specific set of geometrical parameters and operating conditions. It is seen that, due to the available surface superheat exceeding the required superheat for bubble nucleation, ONB is reached very close to the entrance, after which heat transfer coefficient increases sharply. The subcooled boiling regime shows minor changes with local subcooling for  $x_e \leq -0.05$ , after which the slope increases considerably. By using the above-mentioned correction, the slope of subcooled boiling heat transfer coefficient near saturation effectively becomes constant and indicative of the trend of  $h_z$  vs.  $x_e$  observed in the more-subcooled region (to the left;  $x_e \leq -0.05$ ).

### 2.3.3. Saturated Flow Boiling Regime

As discussed in [27], the fluid remains subcooled for all experimental cases and validation of the saturated boiling regime is not needed. But for completeness, four options for calculating heat transfer in the saturated boiling regime are suggested based on validation results from other studies [31,67–69] involving large databases of conventional sized channels and annuli. The four options are: Gungor and Winterton's newer (1987) correlation [67], Gungor and Winterton's older (1986) correlation [30], Shah's chart correlation [70], and Liu and Winterton's correlation [31]. Note that

all correlations recommend the use of liquid Reynolds number,  $Re_f = G(1-x_e)D/\mu_f$ , whereas Liu and Winterton liquid-only Reynolds number,  $Re_{fo} = GD/\mu_f$ . Section 4.1 provides a discussion on the differences in heat transfer trends obtained for each correlation. Unless otherwise mentioned, Gungor and Winterton's (1987) correlation is used with  $D_h$  in this study based on (i) good continuity of  $h$  and  $T_w$  about  $x_e = 0$  (see Fig. 7) and (ii) other correlation evaluation studies [31,69] demonstrating its overall best predictive capability among the four options.

### 2.3.4. Single-phase Vapor Flow Regime

Predictions for this flow regime can be made using the same relations as single-phase liquid fully developed flow but with the liquid properties replaced by those for vapor.

## 3. Experimental Methods and Comparison of Predictions with Experimental Data

### 3.1. Experimental Methods

Before proceeding onto the results of comparison of predictions with experimental data, a brief overview of the experimental methods used to obtain this database is provided.

A schematic diagram of the experimental flow loop indicating key components is shown in Fig. 4(a). The dielectric coolant, HFE-7100, is pumped from a large reservoir by an internal gear pump, through a filter, one among a set of two rotameter flow meters, main control valve, plate-type heat exchanger serving as inlet sub-cooler, and into the test module. The highly subcooled liquid entering the module receives heat from the heater and rises in temperature and/or vaporizes depending on the heat flux. The single-phase liquid/two-phase mixture exiting module is brought down to a lower temperature liquid in a plate-type heat exchanger serving as condenser, and the liquid is returned to the reservoir. A relief valve is provided in the loop for safety and a degassing contactor for removing any dissolved non-condensable gas in the coolant. Both plate-type heat exchangers are provided with their own secondary water loops circulated and conditioned by modular coolers.

The primary component of the horizontally-oriented test module is a 6.35-mm diameter thin custom-built heater to mimic heat generation from a current-carrying wire of the same diameter. Photographs of the module before assembly, honeycomb core holding heater at exact center of outer tube, module after assembly, and insulated module fitted onto experimental facility are respectively shown in Figs. 4(b), 4(c), 4(d), and 4(e). The heater comprises an upstream unheated length, middle heated length, and a downstream unheated length of 88.9 mm, 304.8 mm, and 165.1 mm, respectively. The heater is placed at the exact center of a 23.62-mm tube by fittings on one end and a 6.35-mm thick water-jet-cut aluminum honeycomb core on the other, forming a flow annulus. This core also serves to spread flow streamlines evenly around the annulus. Five thermocouples are silver-soldered onto the Incoloy heater surface at locations 25.4, 88.9, 152.4, 215.9, and 279.4 mm from the start of heated length, to measure surface temperature. The module also contains two sets of thermocouples, analog pressure gauges, and absolute pressure transducers at each end to measure bulk fluid temperatures and absolute pressures. All thermocouples are type-T and calibrated in-house against a standard platinum resistance temperature detector to improve the accuracy to less than  $\pm 0.1^\circ\text{C}$ . Heater power is regulated through an auto-transformer and measured using a power meter. The entire module is insulated with 12.7-mm thick foam to prevent heat losses (see Fig. 4(e)).

A summary of key parameters of the amassed experimental database is presented in Table 4. For more details, the reader is directed to the authors' companion experimental study [27].

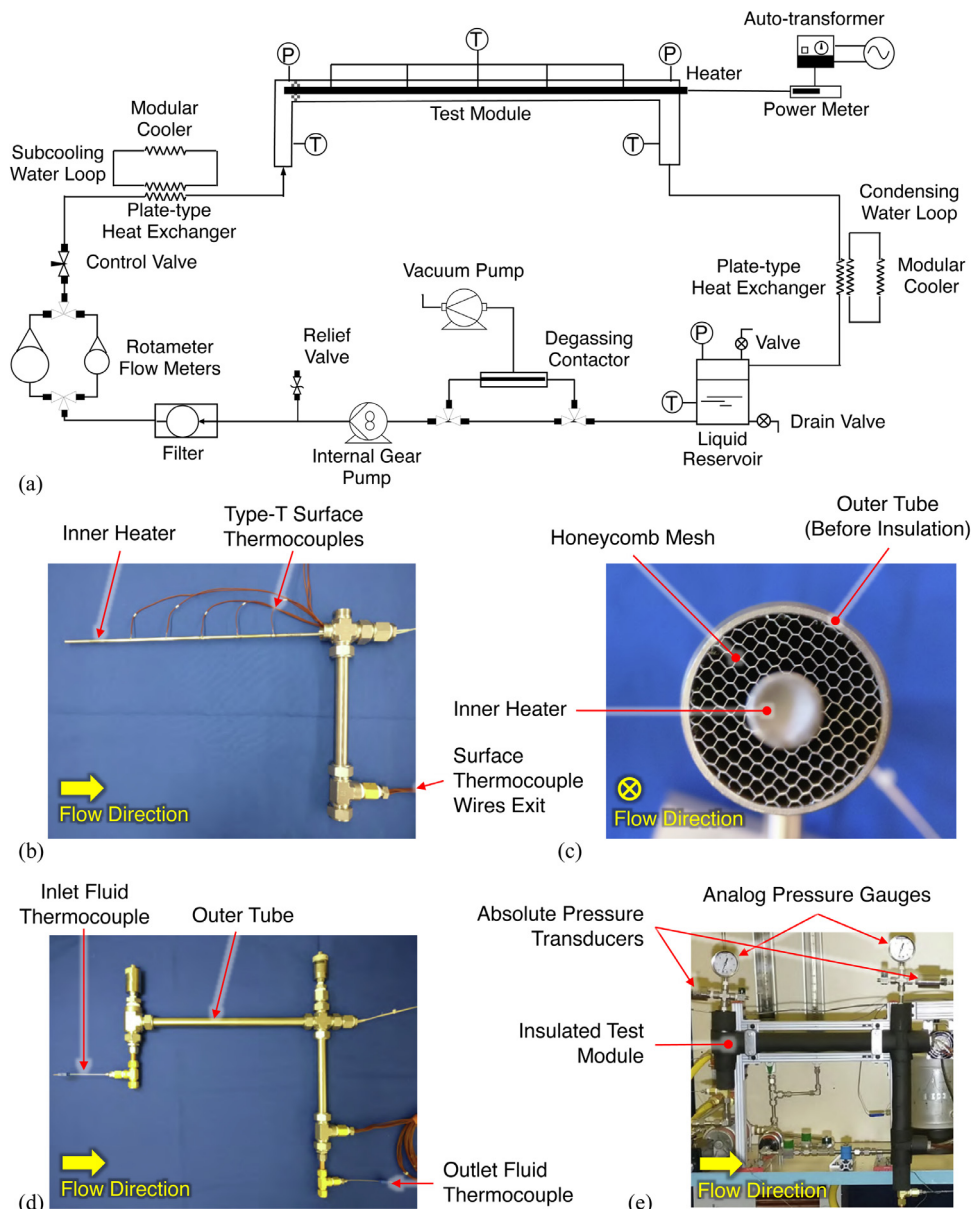


**Fig. 4.** (a) Schematic diagram of experimental two-phase flow loop. Photographs of (b) module before assembly, (c) honeycomb core holding heater at exact center of outer tube, (d) module after assembly, and (e) insulated module fitted onto experimental facility.

**Table 4**  
Summary of key parameters of experimental datapoints from [27].

Fluid	HFE-7100
Mass velocity, $G$	45.51 – 730.50 kg/m <sup>2</sup> s
Volumetric flow rate, $Q_v$	$1.25 \times 10^{-5}$ – $2.02 \times 10^{-4}$ m <sup>3</sup> /s(0.20 – 3.20 gal/min)
Inlet pressure, $P_{in}$	102,999 – 142,392 Pa(14.94 – 20.65 psia)
Outlet pressure, $P_{out}$	102,061 – 140,218 Pa(14.80 – 20.34 psia)
Surface heat flux, $q''_s$	16,309 – 199,210 W/m <sup>2</sup>
Inlet temperature, $T_{in}$	20.33 – 29.23°C
Inlet subcooling, $\Delta T_{sub,in}$	33.83 – 48.68°C
Inlet quality, $x_{e,in}$	-0.516 – -0.349
Outlet temperature, $T_{out}$	21.00 – 44.96°C
Outlet subcooling, $\Delta T_{sub,out}$	17.83 – 47.69°C
Outlet quality, $x_{e,out}$	-0.504 – -0.185
Average surface temperature, $T_s$	36.24 – 96.02°C
Equivalent current through charging wire, $I_{wire}$	725.61 – 2437.91 A

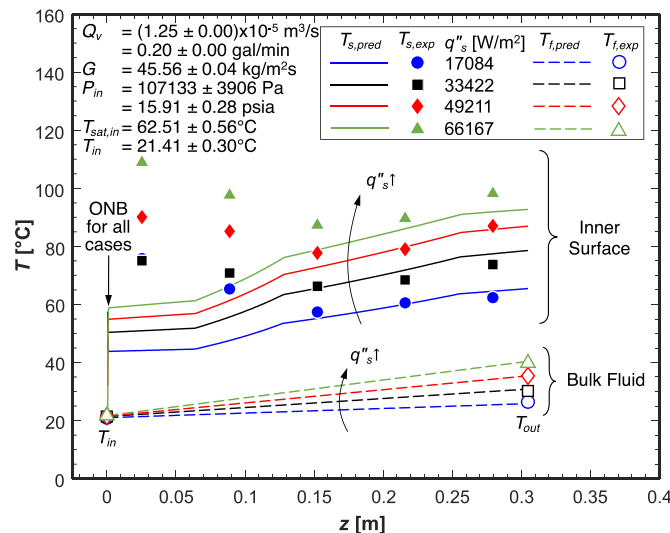


**Fig. 5.** Comparison of consolidated method predictions of inner surface and bulk fluid temperatures to experimental data in the laminar flow regime for different surface heat fluxes.

### 3.2. Comparison of Predictions for Laminar Flows

Fig. 5 shows, for different heat fluxes, comparisons of the consolidated method predictions of inner surface and bulk fluid temperatures to experimental data in the laminar flow regime. This set of operating conditions corresponds to the lowest flow rate experimentally tested and a Reynolds number of  $Re_f = 1469$ . Given the very low mass velocity through the annulus, subcooled boiling commences very close to the inlet. Surface and fluid temperatures are compared to predictions because they are directly measured in experiments and reveal the simultaneous predictive capability of both pressure drop and heat transfer coefficient of the consolidated method. Laminar flows tend to have very long entrance lengths [35], and the length of the experimental module is shorter than the hydrodynamic entrance length, so the flow is simultaneously developing throughout the module. The predicted surface temperature is seen to increase both along the flow direction and with increasing surface heat flux. But the experimental trend is a large surface temperature near the inlet (consider the first two upstream datapoints) and an increase in the downstream part of the module (consider the last three downstream datapoints) with a slope similar to that of the predictions. It is clear that the predictions are in good agreement with experimental data in the downstream part of the module for all heat fluxes. The abnormally high  $T_s$  noticed near the inlet during experiments can be explained by the very low mass velocity in a large diameter annulus. The flow might not be fast enough to remove bubbles nucleating near the entrance and might have resulted in localized vapor pockets near the upstream thermocouple locations. However, this cannot be verified in absence of visual access to the interior of the module during experiments. Since most applications have a much larger  $L_h/D_h$  ratio than shown in Fig. 5, predictive capability in the downstream region matters the most. Moreover, practical applications rarely use such low flow rates in the laminar regime because of their inferior heat transfer performance. For all four  $q''_s$  cases, the inferior heat transfer at such low flow rates results in high  $T_s$ , which exceeds the temperature required for bubble incipience and causes ONB to occur very close to the inlet. Fig. 5 also shows streamwise bulk fluid temperature variations for all heat fluxes. Inlet fluid temperature is used as an input in the prediction method, so the match with experiments is perfect at this location. The predictions yield an almost linear increase in  $T_f$  from the inlet towards the outlet, due to

the constant heat flux emanating from the inner surface and a constant rate of heat addition to the subcooled bulk fluid. This rate of  $T_f$  increase is higher for higher heat fluxes, per basic energy conservation. For all cases, the predicted values of fluid temperature at the outlet are in almost perfect agreement with the measured values; the minor variations can be attributed by the presence of

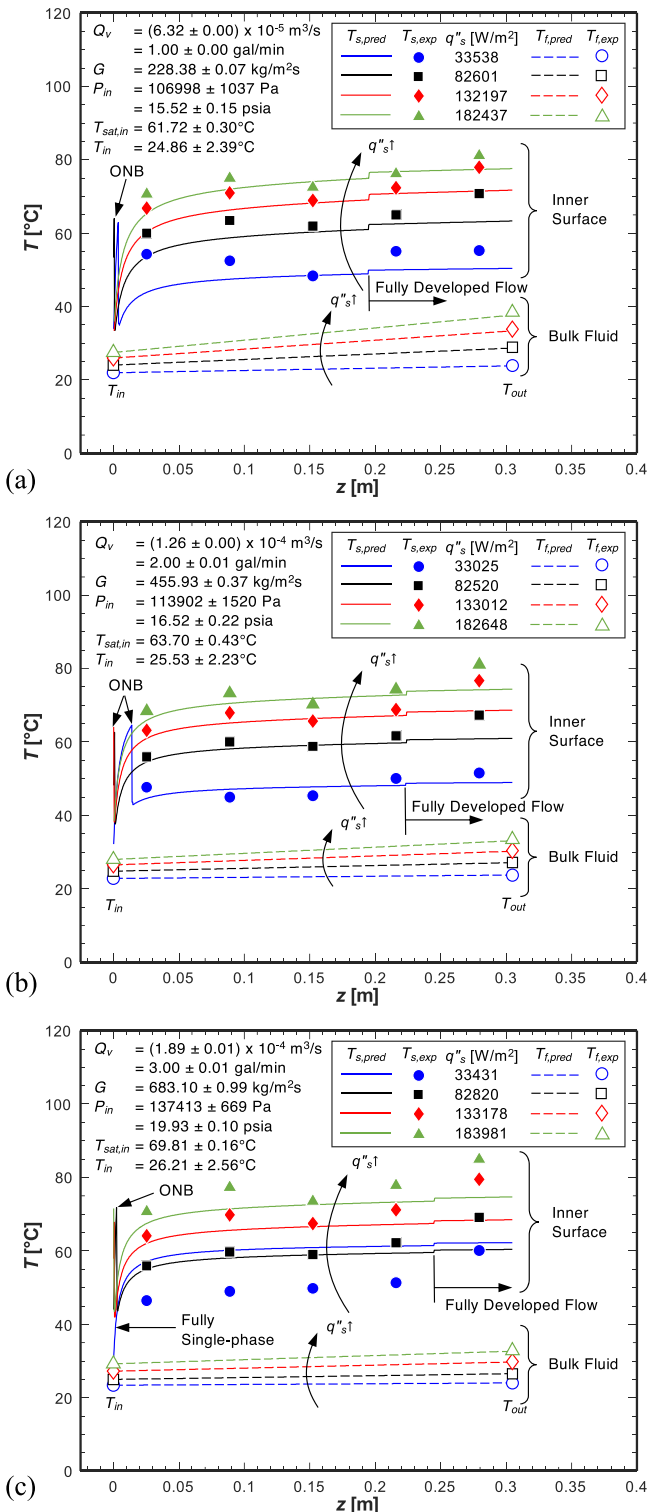


**Fig. 6.** Comparison of consolidated method predictions of inner surface and bulk fluid temperatures to experimental data in the turbulent flow regime for different surface heat fluxes and mass velocities of (a)  $G = 228.38 \text{ kg/m}^2\text{s}$  ( $Q_v = 1.00 \text{ gal/min}$ ), (b)  $G = 455.93 \text{ kg/m}^2\text{s}$  ( $Q_v = 2.00 \text{ gal/min}$ ), and (c)  $G = 683.10 \text{ kg/m}^2\text{s}$  ( $Q_v = 3.00 \text{ gal/min}$ ).

non-condensed vapor in the bulk liquid at  $T_{out}$  measurement location.

### 3.3. Comparison of Predictions for Turbulent Flows

Predictive capability in the turbulent flow regime is of more importance because practical thermal management applications use higher flow rates to achieve superior heat transfer performance. Higher flow rates also ensure gravity independence of the two-phase flow system with less stratification because of the dominance of pump-driven liquid drag effects on bubbles over buoyancy effects within the module [71]. Fig. 6 compares, for different heat fluxes, the consolidated method predictions of inner surface and bulk fluid temperatures to experimental data in the turbulent flow regime for mass velocities of (a) 228.38, (b) 455.93, and (c) 683.10 kg/m<sup>2</sup>s, which correspond, respectively, to flow rates of  $Q_v = (0.63, 1.26, \text{ and } 1.89) \times 10^{-4} \text{ m}^3/\text{s}$  (1.00, 2.00, and 3.00 gal/min), and Reynolds numbers of  $Re_f = 7478, 14,822, \text{ and } 22,219$ . Entrance lengths for all cases are predicted to be shorter than the module length, a characteristic of typical turbulent flows [35]. The bulk fluid temperature,  $T_f$ , increases along the flow direction, and with increasing  $q''_s$ . For all combinations of  $G$  and  $q''_s$ ,  $T_f$  predictions almost perfectly match the experimental values. In Figs. 6(a) and 6(b), sharp reductions in  $T_s$  near the inlet indicate ONB occurrence for the different heat fluxes. This is due to the subcooled boiling heat transfer coefficient being at least an order of magnitude higher than single-phase convection.  $T_s$  is also seen to gradually increase along the flow direction in the subcooled boiling regime, and with increasing  $q''_s$ . The predicted values are in good agreement with those measured. In Fig. 6(c), the surface temperature profiles corresponding to the three higher  $q''_s$  cases are in general agreement with the experimental values. But, while the predicted  $T_s$  profile for the lowest heat flux,  $q''_s = 33,431 \text{ W/m}^2$ , shows a trend similar to that of the measured values, this case shows a clear offset. Notice for this particular case that the consolidated method predicts surface temperature never reaches  $T_{s,ONB}$ , i.e., boiling does not occur and single-phase flow is maintained along the entire module. This is the reason for the blue  $T_s$  curve (lower  $q''_s = 33,431 \text{ W/m}^2$ ) to be higher than the black curve (higher  $q''_s = 82,820 \text{ W/m}^2$ ) wherein ONB occurs near the inlet and causes a drop in surface temperature and clearly indicates the benefit of subcooled flow boiling over single-phase convection. For all three cases, tiny downstream bumps in the predicted  $T_s$  profiles indicate transition to fully developed flow.

Overall, this consolidated predictive method is validated for the entire experimental ranges in Table 4 and the suggested application range is the same. Extrapolation beyond these validation ranges is possible as the individual correlations/models are already applicable for wide ranges, however caution should be exercised. This method could serve as a guide and allows for future modifications for fluids with significantly different thermophysical properties, operating conditions, etc., by substituting appropriate correlations/models.

## 4. Charging Wire Cooling Predictions

The consolidated theoretical/empirical method is adopted to obtain heat transfer and pressure drop predictions for HFE-7100 flow surrounding a copper charging wire of fixed length of  $L_{wire} = 5.00 \text{ m}$  (typical for actual charging cables) through which a continuous current,  $I_{wire}$ , is passed. Effects of various important parameters that aid in the final system design are discussed in this section. The geometry and operating conditions for which predictions are made are described in the figures to follow. All flow rates considered are high enough to maintain turbulent flow with high Reynolds numbers. It is re-emphasized that the consolidated

method does not consider flow stratification effects nor is it intended for CHF prediction. As discussed in [27], the relation between the charging wire current and surface heat flux is

$$q''_s = \begin{cases} \frac{I_{wire}^2 \rho_{20^\circ\text{C}} (1 + \alpha(T_s - 20^\circ\text{C}))}{(\pi^2/4) D_{wire}^3} & , T_s \geq 20^\circ\text{C} \\ \frac{I_{wire}^2 \rho_{20^\circ\text{C}}}{(\pi^2/4) D_{wire}^3} & , T_s < 20^\circ\text{C} \end{cases}, \quad (1)$$

where  $\rho_{20^\circ\text{C}}$  is the conductor resistivity at 20°C and  $\alpha$  the conductor temperature coefficient. In the predictions to follow, Eq. (1) is coupled with the relations given in Tables 2 and 3.

### 4.1. Choice of Saturated Boiling Regime Heat Transfer Correlation

Fig. 7 shows predictions of four different heat transfer coefficient correlations for the saturated boiling regime for the same set of operating conditions. Given the low flow rate of  $Q_v = 6.31 \times 10^{-5} \text{ m}^3/\text{s}$  (1.00 gal/min) to cool a wire carrying a high current of 2000 A, the fluid reaches saturation ( $x_e = 0$ ) midway along the annulus. Since the same methodology is used to predict heat transfer and pressure drop in the upstream flow regimes, the local temperature and pressure profiles overlap onto one another until saturation. In Fig. 7(a), the sharp decrease in  $T_s$  near the inlet represents ONB, as discussed earlier. The reason for the sharp decrease is the discontinuity in the heat transfer coefficients predicted in the pure single-phase liquid regime and the subcooled boiling regime. Following ONB, the heat transfer coefficient increases abruptly (by about an order of magnitude) as the first bubbles begin nucleating because of the dominance of latent over sensible heat transfer. The minute bump in  $T_s$  at around  $z = 0.2 \text{ m}$  indicates the predicted point of development of both velocity and thermal boundary layers. Owing to the increase in subcooled boiling heat transfer coefficient as the local subcooling decreases, the difference between  $T_f$  and  $T_s$  keeps decreasing downstream. The fluid increases in temperature in a linear fashion until it reaches saturation. The change in trend of  $T_s$  in the region  $-0.05 < x_e < 0$  is the outcome of the correction described in section 2.3.2. Fig. 7(b) shows pressure drop in the subcooled boiling region is much smaller than in the saturated boiling region. The rapid pressure drop in the region  $x_e \geq 0$  causes a corresponding decrease in  $T_f$ . There is no significant difference in pressure drop predictions due to the choice of  $h_{sb}$  correlation. Any small differences can be explained by changes in local fluid properties. This also causes the  $T_f$  profiles in the saturated region to fall onto one another.

In Fig. 7(a),  $T_s$  again abruptly changes depending on the choice of  $h_{sb}$  correlation. With  $T_f$  being almost the same for all cases, it is easy to compare saturated boiling heat transfer coefficients from the  $T_s$  profiles, the higher the  $T_s$ , the lower the predicted heat transfer coefficient. It is seen that Gungor and Winterton's (1987) [67] correlation seems to predict in a continuous fashion. They suggested use of heated perimeter diameter,  $D_{hp}$ , for better predictions with their correlation for annuli; although the effect of choice of length scale,  $D$ , is not explicitly evident in the correlation, the effect is incorporated in the form of different  $Re$ , which affects the single-phase heat transfer coefficient and then the saturated boiling heat transfer coefficient. This yields a slightly higher  $T_s$  (or lower  $h$ ) than using  $D_h$  but follows the same trend of  $T_s$  increase downstream. A similar trend, but with  $T_s$  values lower than Gungor and Winterton (1987) is obtained using their older (1986) [30] correlation. It is to be noted that although the trends ended up being similar, the forms of these two correlations are very different. Liu and Winteron's [31] correlation predicts a fairly constant heat transfer coefficient along the entire saturated boiling region, making  $T_s$  decrease along the flow direction in accordance

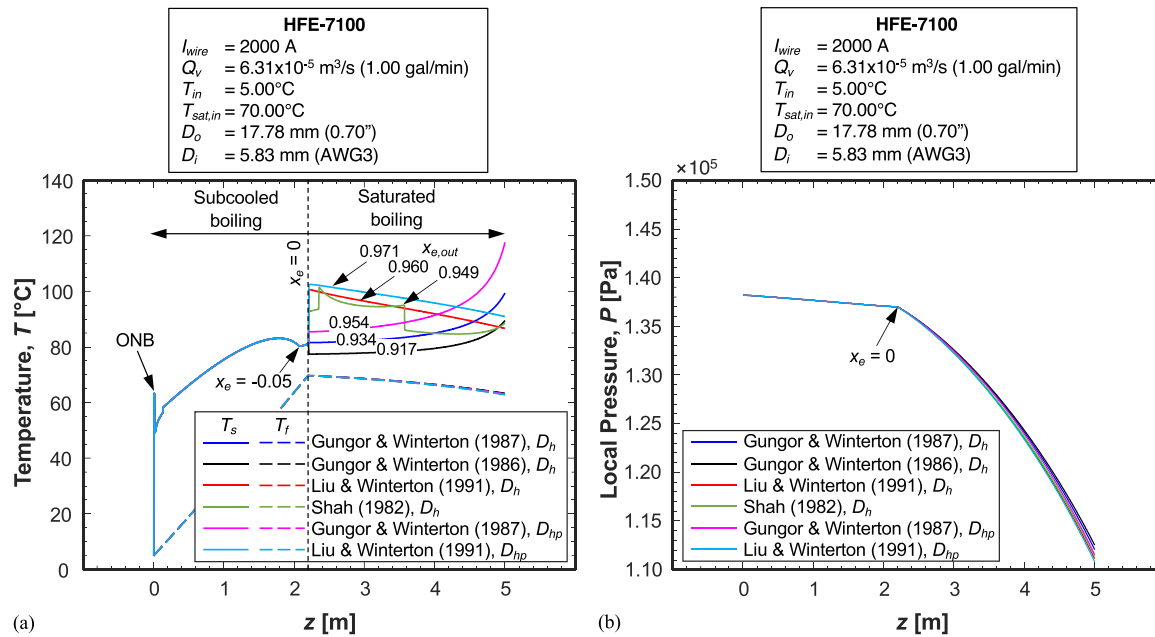


**Fig. 7.** Predictions of (a) local surface and fluid temperatures, and (b) pressure profiles based on different saturated flow boiling heat transfer correlations.

with  $T_f$ . Using  $D_{hp}$  instead of  $D_h$  in their correlation increases the surface temperature. Shah's [70] chart correlation divides the saturated boiling regime into three parts and therefore yields discontinuous predictions. The major reason for the different correlations exhibiting predominantly two trends in  $T_w$  (Liu and Winterton decreasing and the others increasing streamwise) within the saturated boiling region are the choice of Reynolds number used. Liu and Winterton recommend the use of liquid-only Reynolds number,  $Re_f = GD/\mu_f$ , which remains constant as  $x_e$  increases along streamwise direction, making  $h$  almost constant, and  $T_w$  follow the same slope as  $T_f$ . The other correlations recommend the use of liquid Reynolds number,  $Re_f = G(1-x_e)D/\mu_f$ , which decreases towards zero downstream, causing  $h$  to decrease and  $T_w$  to increase. Also note the Gungor and Winterton [30,67] and Shah [70] correlations

contain a  $x_e/(1-x_e)$  term raised to a positive power; this term tends toward singularity as  $x_e \rightarrow 1$ . Notice in Fig. 7(a) that all the correlations considered predict exit qualities corresponding to nearly pure vapor, which points to the likelihood of CHF occurrence within the annulus length and probable unsafe operation for these operating conditions and geometrical parameters (refer to section 4.8.2 for discussion on CHF).

Although operating conditions in actual EV charging situations would be selected to maintain subcooled conditions along the entire length of the cable, some of the operating conditions discussed in the later sections do contain a short saturated boiling region. Gungor and Winterton's (1987) [67] correlation will be used with  $D_h$  to predict the saturated boiling heat transfer coefficient henceforth in this study (reason given in section 2.3.3).

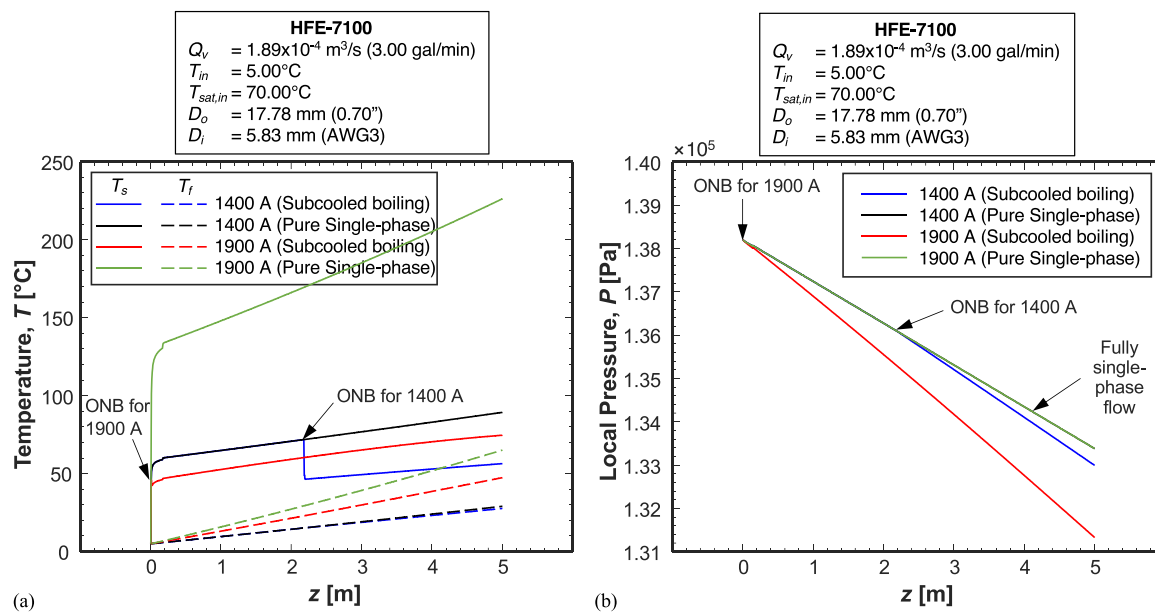


**Fig. 8.** Effectiveness of subcooled boiling over single-phase liquid convection for  $I_{wire} = 1400$  and 1900 A: (a) surface and fluid temperature profiles, and (b) pressure profiles.

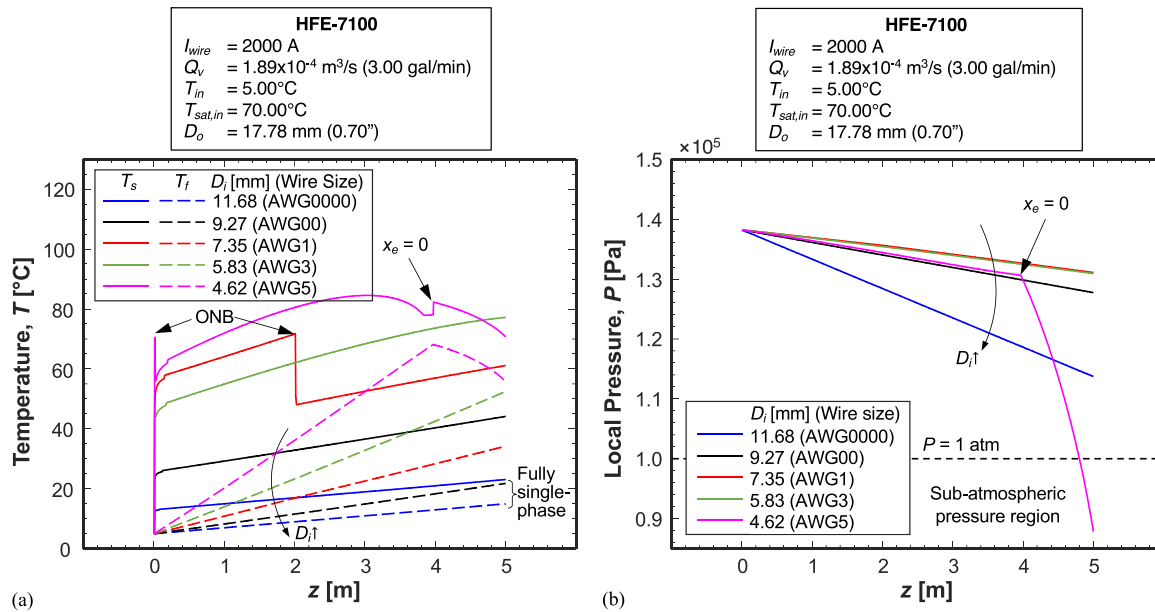


**Fig. 9.** Effects of annulus inner diameter (wire size) on (a) surface and fluid temperature profiles, and (b) pressure profile for fixed outer diameter (conduit size).

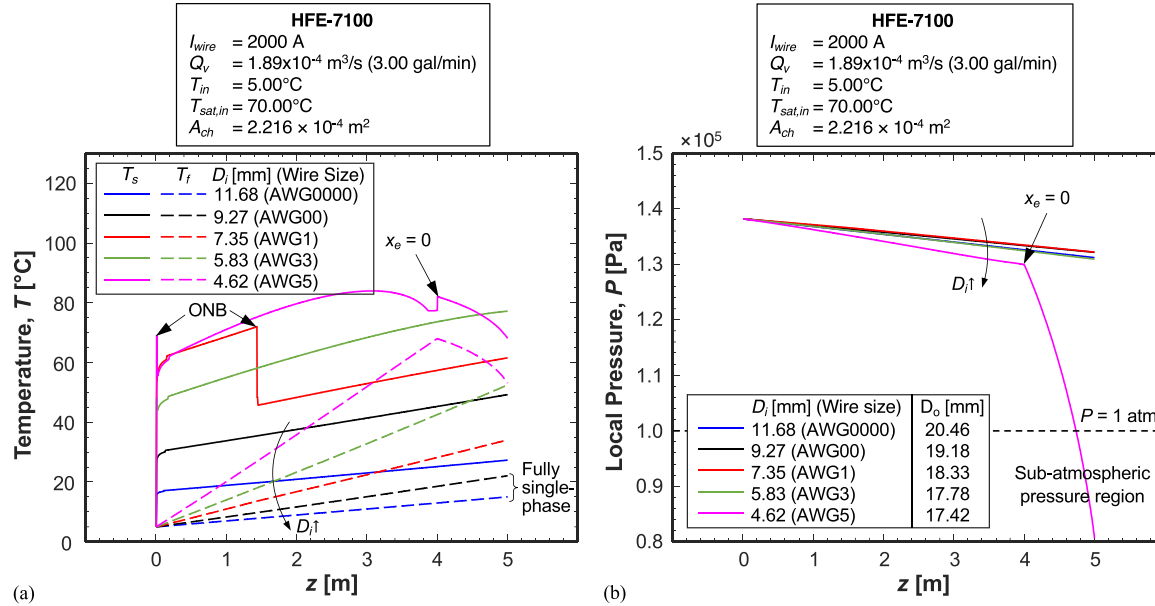


**Fig. 10.** Effects of annulus inner diameter (wire size) on (a) surface and fluid temperature profiles, and (b) pressure profile for fixed flow area.

#### 4.2. Effectiveness of Subcooled Boiling over Single-phase Liquid Convection

Fig. 8 elucidates the effectiveness of subcooled boiling over single-phase heat transfer for  $I_{\text{wire}} = 1400$  and 1900 A. The same consolidated method, operating conditions, and fluid properties are used for both, but for obtaining pure single-phase predictions, the ONB criterion is artificially turned off. The operating conditions considered here ensure subcooled liquid outlet. It can be seen in Fig. 8(a) that, for single-phase flow,  $T_s$  maintains a trend almost parallel to that of  $T_f$  in the fully developed flow region because of the almost constant heat transfer coefficient of pure liquid convection. For the same set of operating conditions, subcooled boiling decreases  $T_s$  considerably. This is more evident for the higher charging current,  $I_{\text{wire}} = 1900$  A, where  $HFE-7, T_{s,max} = 74.58^\circ\text{C}$  compared to  $T_{s,max} = 226.20^\circ\text{C}$  for single-phase cooling. The latter very

high  $T_{s,max}$  proves that single-phase cooling is obviously unrealistic and unsafe for high charging currents. For  $I_{\text{wire}} = 1400$  A, ONB for the saturated boiling case occurs about halfway along the annulus, after which subcooled boiling brings  $T_s$  down, whereas pure single-phase convection causes a continuous increase in  $T_s$ . Subcooled boiling also results in a cooler fluid at the outlet. Fig. 8(b) shows the pressure profiles for both single-phase cases are fairly linear along the flow direction and completely overlap with one another. And subcooled boiling results in a higher pressure drop downstream of ONB. The total pressure drop,  $\Delta P$ , is 4826 Pa for both single-phase cases, but for subcooled boiling,  $\Delta P$  is 5214 and 6879 Pa for 1400 and 1900 A, respectively, which correspond to 8.04% and 42.54% increases compared to the single-phase cases. These  $\Delta P$  increases are relatively manageable in practical situations considering the corresponding enormous corresponding heat transfer enhancement with subcooled flow boiling.

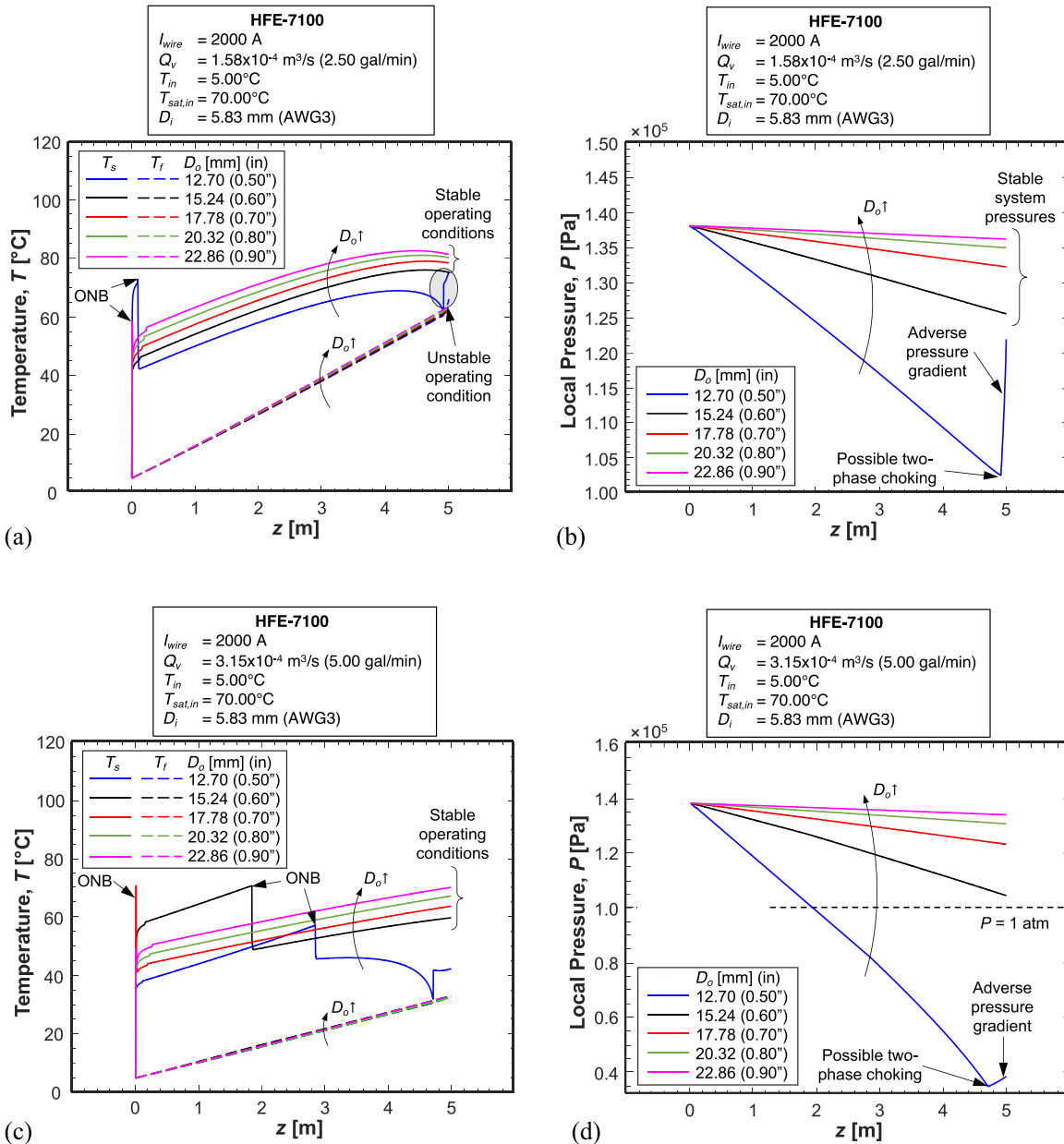


**Fig. 11.** Effects of annulus outer diameter (conduit size) with fixed wire size on (a) surface and fluid temperature profiles and (b) pressure profile for  $Q_v = 1.58 \times 10^{-4} \text{ m}^3/\text{s}$  (2.50 gal/min), and (c) surface and fluid temperature profiles and (d) pressure profile for  $Q_v = 3.15 \times 10^{-4} \text{ m}^3/\text{s}$  (5.00 gal/min).

#### 4.3. Annulus Inner Diameter (Wire Size)

Standards are available worldwide for the maximum current through different sizes of air-cooled electrical conductors. For free-air-cooled wires, oversizing the conductor is usually not a problem. However, this is not the case in many practical applications involving stringent volume and weight limits. Fig. 9 shows, for a fixed annulus outer diameter (conduit size) of  $D_o = 17.78$  mm and a relatively high current of  $I_{\text{wire}} = 2000$  A, the effects of annulus inner diameter (wire size),  $D_i$ , on heat transfer and pressure drop characteristics of the cooling scheme. Shown are results for five different standard American Wire Gauge (AWG) sizes: 0000, 00, 1, 3, and 5. Fig. 9(a) shows that for the two largest wire sizes, AWG0000 and AWG00, the flow remains single-phase liquid. With  $D_o$  and flow rate held constant, a larger  $D_i$  both decreases the flow area and increases the mass velocity. Additionally, Eq. (1) shows the heat flux varies as the cube root of  $D_i$ . The combination of higher mass ve-

locity and/or higher heat flux leads to comparatively low values for both  $T_f$  and  $T_s$  for larger wire sizes. For the smallest wire size, AWG5, the opposite is observed, and the fluid reaches saturation conditions. The intermediate wire sizes of AWG1 and AWG3 acquire subcooled boiling, with AWG1 having ONB downstream of that for AWG3. Fig. 9(b) shows how, because of appreciable vapor generation, pressure drop for AWG5 is so large that the local pressure near the outlet goes sub-atmospheric, which is undesired due to possibility of air inclusion into the HFE-7100 in actual charging situations. For the other wire sizes, pressure drop increases considerably with increasing wire diameter because of smaller hydraulic diameter and increased flow velocity. Overall, AWG3 provides a good comprise of (i) both low surface and fluid temperatures, (ii) small pressure drop, (iii) good flexibility, and (iv) lightweight cables.

Another method to help isolate the effect of  $D_i$  is to compare results for fixed flow area,  $A_{ch}$ , (and also fixed mass velocity) rather

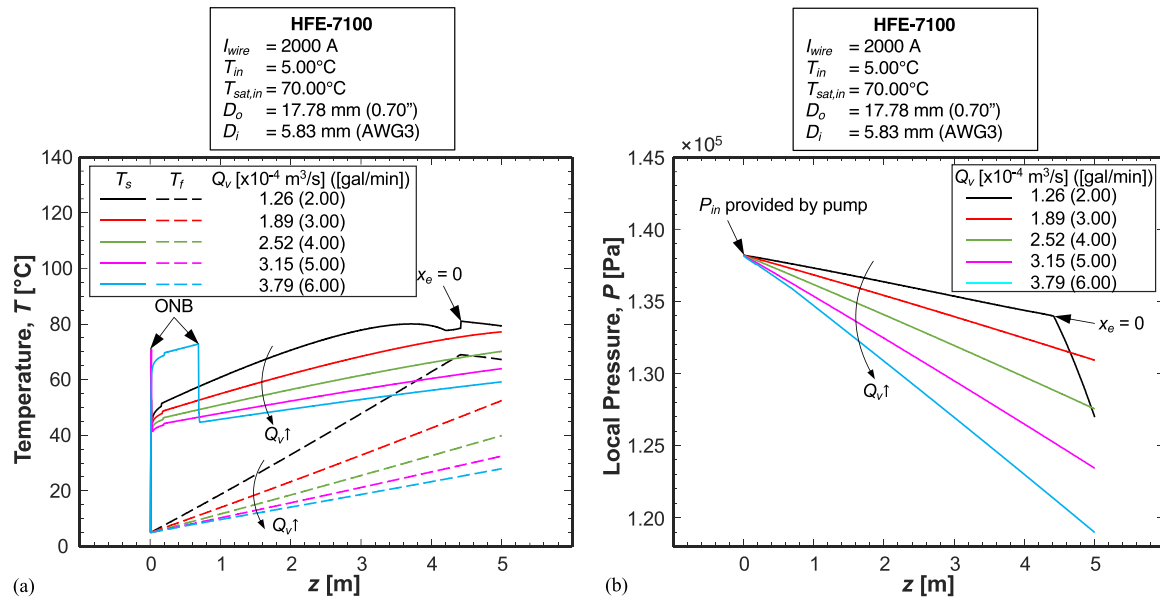


Fig. 12. Performance of cooling system for  $I_{\text{wire}} = 2000 \text{ A}$  and different flow rates: (a) surface and fluid temperature profiles and (b) pressure profile.

than fixed  $D_o$ . This would help determine the reason for trends in Fig. 9(a), i.e., whether  $G$  or  $q''_s$  contribute more to the trends with respect to  $D_i$ . Fig. 10 shows trends for a fixed flow area of  $A_{ch} = 2.216 \times 10^{-4} \text{ m}^2$  (equal to that of AWG3 and  $D_o = 17.78 \text{ mm}$  in Fig. 9) with all other parameters the same as in Fig. 9. The trends in Fig. 10(a) resemble those of Fig. 9(a) but with slight differences. It is clear that both  $G$  and  $q''_s$  contribute to heat transfer trends with respect to  $D_i$ , with the larger contribution from  $q''_s$ . Fig. 10(b) shows pressure profile is about the same for the four largest wires because of equal mass velocity and small amount of vapor generated along the annulus (including zero vapor generation for AWG0000) in the single-phase and subcooled boiling regions. Like Fig. 9(b), pressure drop for AWG5 in Fig. 10(b) is quite large and leads to sub-atmospheric conditions in the outlet region.

#### 4.4. Annulus Outer Diameter (Conduit Size)

Figs. 11(a) and 11(b) illustrate the effects of outer diameter (or conduit size),  $D_o$ , on local surface and fluid temperature profiles and pressure profile, respectively, for a fixed inner diameter of  $D_i = 5.83 \text{ mm}$  (AWG3) and a relatively low flow rate of  $Q_v = 1.58 \times 10^{-4} \text{ m}^3/\text{s}$  (2.50 gal/min). Five different conduit sizes are compared. Although smaller  $D_o$  is preferred for EV charging in terms of both weight and cable flexibility, Figs. 11(a) and 11(b) show the smallest outer diameter of  $D_o = 12.70 \text{ mm}$  renders the system unstable because of two-phase choking. Choking is manifest as a steep adverse pressure gradient, which is seen near the outlet in Fig. 11(b). This condition, which accounts for both two-phase flashing and compressibility effects, is accurately determined using HEM [33]. The flow is stable for other outer diameters. ONB is encountered near the entrance for all  $D_o$ , and subcooled boiling occurs along the entire wire length. There are no significant differences in  $T_f$  among the different  $D_o$  cases, but pressure drop decreases with increasing  $D_o$  because of the decreasing mass velocity.

Figs. 11(c) and 11(d) present results for a higher flow rate of  $Q_v = 3.15 \times 10^{-4} \text{ m}^3/\text{s}$  (5.00 gal/min). Here, the smallest of  $D_o = 12.70 \text{ mm}$  shows a massive pressure drop culminating in sub-atmospheric pressure conditions for more than half the flow length as well as two-phase choking near the outlet. Pressure drop again increases with decreasing  $D_o$ , but the differences are larger than in

Fig. 11(b) because of the higher flow rate. ONB moves downstream with decreasing  $D_o$  because of the increasing mass velocity. And the outlet fluid temperature remains almost constant for all cases.

#### 4.5. Performance at Different Flow Rates

Fig. 12 shows the performance of the cooling system for  $I_{\text{wire}} = 2000 \text{ A}$  and different flow rates in the range of  $Q_v = (1.26 - 3.79) \times 10^{-4} \text{ m}^3/\text{s}$  (2.00 – 6.00 gal/min). Fig. 12(a) shows  $T_f$  increasing with decreasing  $Q_v$ . For the lowest flow rate of  $Q_v = 2.00 \text{ gal/min}$ , the fluid reaches saturation temperature, causing saturated boiling to occur downstream. For all  $Q_v$  values, ONB occurs at the inlet, except for the highest flow rate of  $Q_v = 6.00 \text{ gal/min}$ , for which there is a short single-phase portion near the inlet. And both  $T_s$  and  $T_f$  for all flow rates lie in a reasonably safe range. Fig. 12(b) shows pressure drop generally increases with increasing flow rate except for the lowest flow rate of  $Q_v = 2.00 \text{ gal/min}$ , for which pressure drop is higher because of the downstream saturated boiling.

#### 4.6. Inlet Fluid Temperature

Figs. 13(a) and 13(b) illustrate the effects of inlet fluid temperature on the performance of the cooling system for  $I_{\text{wire}} = 2000 \text{ A}$ . With the inlet saturation temperature held constant, these figures also show the effect of inlet subcooling in the range of  $\Delta T_{sub,in} = 40.00 - 80.00^\circ\text{C}$ . Fig. 13(a) shows that, for all cases, ONB occurs close to the inlet and  $T_f$  profiles are almost parallel to one another. And  $T_s$  profiles are almost parallel for lower values of  $T_{in}$  (higher  $\Delta T_{sub,in}$ ), with maximum variation along the flow direction achieved at the highest  $T_{in}$  (lowest  $\Delta T_{sub,in}$ ). For most part of the flow length  $T_s$  increases with increasing  $T_{in}$ . Fig. 13(b) shows pressure drop is higher for higher  $T_{in}$  (lower  $\Delta T_{sub,in}$ ).

Figs. 13(c) and 13(d) show comparative effects of  $T_{in}$  for the same geometry and operating conditions, but a lower current of  $I_{\text{wire}} = 1500 \text{ A}$ . Clearly captured in Fig. 13(a) is the upstream shift of ONB with increasing  $T_{in}$  (decreasing  $\Delta T_{sub,in}$ ), which is the outcome of the superheat required to induce bubble incipience decreasing with decreasing  $\Delta T_{sub,in}$ .

Fig. 14 shows the effects of inlet subcooling on average heat transfer coefficient and average surface temperature. It is noted

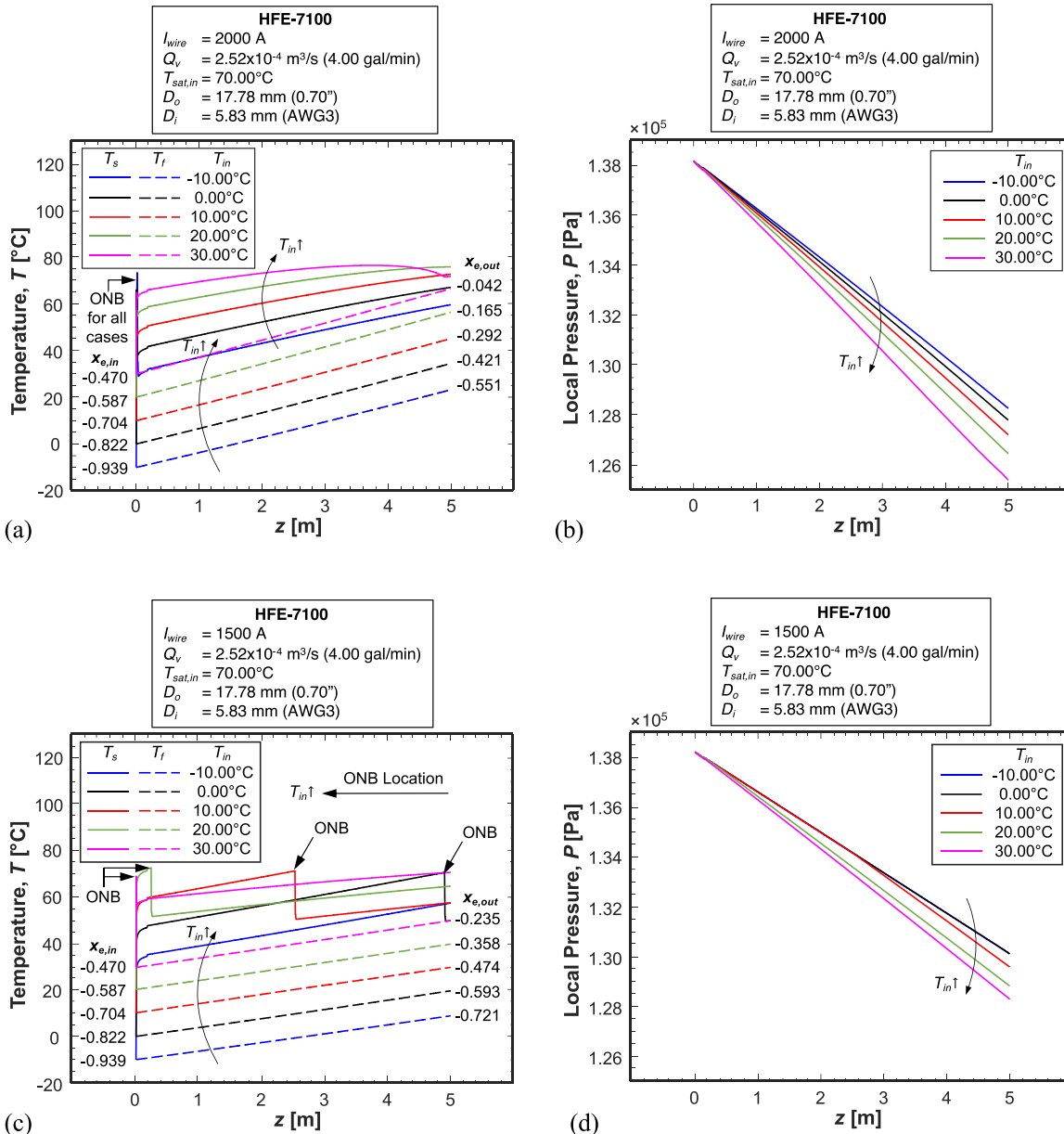


**Fig. 13.** Effects of inlet fluid temperature on performance of cooling system: (a) surface and fluid temperature profiles and (b) pressure profile for  $I_{wire} = 2000$  A, and (c) surface and fluid temperature profiles and (d) pressure profile for  $I_{wire} = 1500$  A.

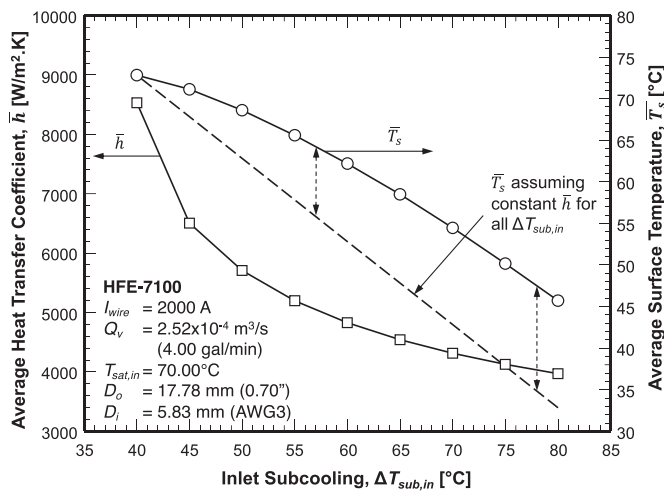


**Fig. 14.** Variation of average heat transfer coefficient and average surface temperature with inlet subcooling for  $I_{wire} = 2000$  A.

that the subcooled boiling regime occupies the entire length for all the  $\Delta T_{sub,in}$  values considered here. The average heat transfer coefficient decreases with increasing  $\Delta T_{sub,in}$ , which is consistent with the experimental results of Lie and Lin [72]. Notice that the profiles of both the average heat transfer and average surface temperature are non-linear, and increasing  $\Delta T_{sub,in}$  (supplying the liquid at lower temperature) does not reduce average  $T_s$  by the same amount. For example, increasing  $\Delta T_{sub,in}$  from 60.00 to 80.00°C (i.e., by 20.00°C) leads to reduction in average  $T_s$  from 62.19 to 45.71°C (i.e., by 16.48°C).

#### 4.7. Performance for Different Charging Wire Currents

**Fig. 15** shows the performance of the cooling system for fixed geometry and operating conditions, but different currents flowing through the wire. It can be seen in **Fig. 15(a)**, that for  $I_{wire} = 500$  and 1000 A, the flow remains single-phase liquid all along the an-

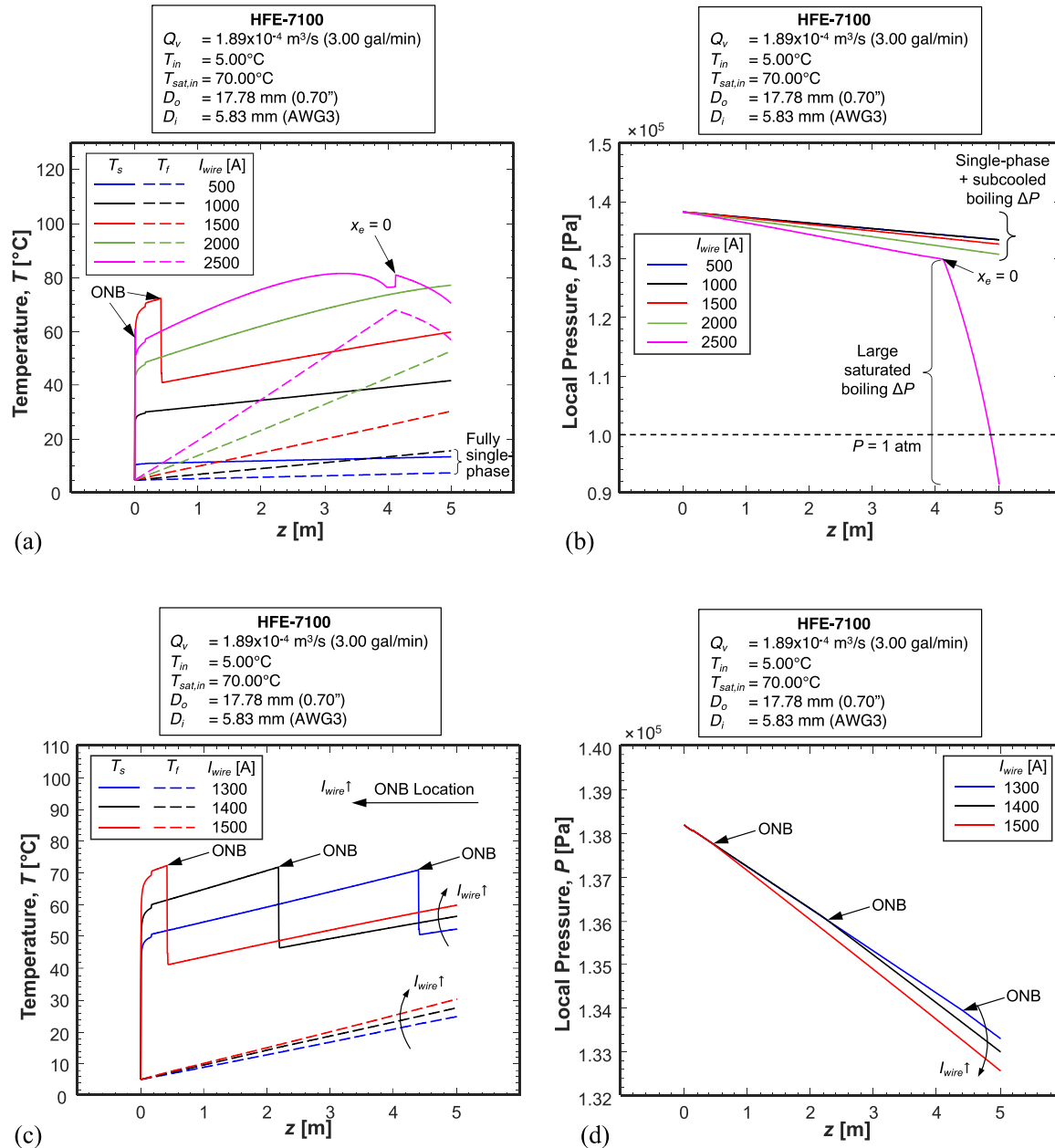


**Fig. 15.** Performance of cooling system for different charging currents. (a) Surface and fluid temperature profiles and (b) pressure profile for  $I_{\text{wire}} = 500 - 2500$  A. (c) Surface and fluid temperature profiles and (d) pressure profile for  $I_{\text{wire}} = 1300 - 1500$  A.

nulus. For  $I_{\text{wire}} = 1500$  A, the flow is single-phase for a short length upstream, and ONB occurs at the inlet for  $I_{\text{wire}} = 2000$  and 2500 A. The fluid undergoes only subcooled boiling for 2000 A, but 2500 A causes the fluid to reach saturation conditions before the outlet. Fig. 15(b) shows pressure drop is quite small for all cases except 2500 A, where the pressure drop is very large and causes the flow near the outlet to fall below atmospheric pressure. Figs. 15(c) and 15(d) provide results similar to those in Figs. 15(a) and 15(b), respectively, but for a narrow range of  $I_{\text{wire}} = 1300 - 1500$  A. Fig. 15(c) shows how ONB moves upstream with increasing  $I_{\text{wire}}$ . This trend is the outcome of higher current increasing both the surface heat flux and wall superheat, thereby aiding earlier activation of nucleation sites. Fig. 15(d) shows slight deviations from initially linear pressure profile occurring downstream from ONB location as the flow transitions from single-phase liquid to subcooled boiling.

#### 4.8. Additional Considerations

##### 4.8.1. Parallel versus Serial Cooling

The predictions in Figs. 7 – 15 are for a typical 5.00-m long wire. A typical DC charging cable contains two high current carrying wires, which both need to be cooled. In the final thermal management system, the coolant could flow around both these wires along the same (parallel) direction or in opposite (serial) direction; the latter would have the coolant flowing around one wire toward the charging plug and returning around the other wire toward the charging station. The present predictions are equally valid for a parallel-fed 5.00-m long cable, but the total flow rate would be twice what is indicated in the plots. The predictions are also valid for a serial-fed 2.50-m long cable, albeit some errors, such as increased pressure drop due to the flow encountering a 180° bend, are possible.

#### 4.8.2. Critical Heat Flux

Critical Heat Flux (CHF) marks the upper limit of the nucleate boiling regime and therefore represent an upper design limit for all heat-flux controlled applications. Therefore, operating conditions in the two-phase thermal management system must be configured to ensure operation below this limit to realize the aforementioned advantages of high heat transfer coefficients and low surface temperatures. Above CHF, the wire temperature is expected to rise in an unsteadily manner to dangerous levels. Developing experimentally validated CHF relation for annuli is beyond the scope of this study but warrants systematic future study. However, based on extensive evidence for conventional channel flows, CHF is typically seen for  $x_e$  well below unity and may be enhanced by decreasing inlet fluid temperature, increasing flow rate, and reducing heated length.

#### 4.8.3. Charging Wire Stranding

All predictions provided above are based on the assumption of perfectly cylindrical wire with a uniform smooth surface. But both AC and DC wires are often stranded, *i.e.*, made of multiple thinner filaments that are twisted together. This is typically done to increase flexibility of the cable. Stranding leads to formation of gaps within a roughly cylindrical shape. If the wire is directly exposed to the coolant, the fluid would easily fill these voids, given the highly wetting (low contact angle) characteristic of dielectric coolants. To make rough predictions for a stranded wire, a simple correction would be to use a composite thermal conductivity instead of thermal conductivity of the conductor alone. The composite thermal conductivity would be based on conductor void fraction in a circular cross-section, and both conductor and coolant thermal conductivities.

#### 4.8.4. External Temperature of Conduit

The design of a practical EV charger cooling system must consider external temperature of conduit to ensure safe consumer handling. This can be determined by a simple heat rate calculation across the conduit, which is a function of conduit wall thickness and thermal conductivity, and external air natural convection. Since fluid is directly in contact with the conduit's interior surface, an initial rough estimate of conduit wall temperature can be based on the highest value of  $T_f$  for a given current, conduit geometry, and operating conditions.

#### 4.8.5. Charging Cable Length

Finally, an important design conclusion from the results provided in the present study is to reduce length of the charging cable. A shorter cable would ensure operation within the subcooled boiling regime, thereby yielding low surface temperatures and low pressure drops and also helping avoid CHF and two-phase choking. However, any reduction in charge cable length must involve careful consideration of the consumer's handling.

### 4.9. Future Improvements to Predictive Methodology

The present study showed the great difficulty identifying appropriate predictive relations for the different flow regions encountered along the conduit's length, especially those for the subcooled boiling region. Given below are specific recommendations for future work, which would improve predictions for charging cable cooling:

- 1 Develop more accurate and robust instrumentation and data processing methods for measurement of low void fraction in the subcooled boiling regime.
- 2 Explore effects of variations in cable orientation relative to gravity on both heat transfer performance and pressure drop [73,74].

- 3 Capitalize on findings from recent theoretical and computational efforts, which have shown significant successes in modeling interfacial behavior, heat transfer characteristics, and pressure drop in both boiling [75] and condensing [76,77] flows.
- 4 Develop CHF criteria/models for subcooled flow boiling in annuli.

## 5. Conclusions and Design Recommendations

This study explored a thermal management scheme for ultra-fast electric vehicle charging cables using subcooled flow boiling. A consolidated theoretical/empirical method for predicting the heat transfer and pressure drop characteristics for flow through a concentric circular annulus with uniformly heated inner wall and adiabatic outer wall is proposed. This method is capable of tackling both laminar and turbulent flows in all heat transfer regimes, including single-phase liquid, subcooled boiling, saturated boiling, and single-phase vapor. Special attention is paid to entrance effects, given the large values for both conventional-sized annuli and laminar flows. On comparison with subcooled boiling experimental data from the authors' companion study [27], the method shows overall reasonable capability of predicting local surface and fluid temperatures over a wide Reynolds number range. By adopting the prediction method to the EV charger application, predictions are made for a 5.00-m long charging wire and the effects of several parameters on system performance demonstrated to aid in the design and optimization of the final cooling system. Based on the prediction results, the following recommendations are made:

- (i) All design parameters should be selected so that the flow regime along the conduit is predominantly subcooled boiling.
- (ii) The charging cable should be as short as practically permissible.
- (iii) Effects of geometry and flow rate can be combined into those of mass velocity. High mass velocities, while considered to provide better heat transfer performance, will result in large pressure drop and therefore high pumping power. Very high mass velocities might also cause two-phase choking, resulting in unstable and dangerous operation. On the other hand, low mass velocities might cause the flow to reach saturation conditions accompanied by large pressure drop or trigger an early CHF; they may also increase buoyancy effects. As mass velocity has a smaller effect on heat transfer performance in the subcooled boiling regime, an optimal medium mass velocity should be adopted that is capable of maintaining steady subcooled boiling all along the charging wire.
- (iv) An optimal medium value for volumetric flow rate, which is proportional to mass velocity, must be selected based on the geometry. The cooling system should be designed with a pumping capability corresponding to the highest current value. Flow rate could be dynamically adjusted while the system is in operation based on actual current during the charging process.
- (v) For fixed conduit size and flow rate, a larger wire increases mass velocity but reduces flexibility and maneuverability of the charging cable. A smaller wire on the other hand offers better handling, but the resulting higher surface heat flux and lower mass velocity might result in saturated flow boiling, very high pressure drop, and even sub-atmospheric local pressures. An optimal intermediate wire size should therefore be adopted.
- (vi) For fixed wire size and flow rate, a larger conduit decreases mass velocity and increases cable size, and vice versa. An optimal intermediate value should therefore be adopted.
- (vii) Effects of inlet fluid temperature and inlet pressure are collectively reflected in the effect of inlet subcooling. Higher inlet subcooling decreases both average surface temperature and heat transfer coefficient, and vice versa. But maintaining higher inlet subcooling would require higher inlet pressure, and there-

fore higher pumping power, or lower inlet liquid temperature, the latter necessitating additional cooling capability at the charging station. An optimal subcooling range must therefore be adopted based on the maximum allowable cable surface temperature and the ambient temperature.

## Declaration of Competing Interest

None. The authors declare that they have no known competing financial interests or personal relationships that could have appeared to influence the work reported in this paper.

## Acknowledgement

The authors acknowledge the support of the Ford – Purdue University Alliance under grant no. 40002059.

## References

- [1] R. Collin, Y. Miao, A. Yokochi, P. Enjeti, A. Von Jouanne, Advanced electric vehicle fast-charging technologies, *Energies* 12 (10) (2019) 1839, doi:[10.3390/en12101839](https://doi.org/10.3390/en12101839).
- [2] D. Hall, N. Lutsey, Emerging best practices for electric vehicle charging infrastructure, White Paper, The International Council on Clean Transportation, Washington, DC, USA, 2017 White Paper.
- [3] T. Donato, F. Licci, A. D'Elia, G. Colangelo, D. Laforgia, F. Ciancarelli, Evaluation of emissions of CO<sub>2</sub> and air pollutants from electric vehicles in Italian cities, *Appl. Energy* 157 (2015) 675–687, doi:[10.1016/j.apenergy.2014.12.089](https://doi.org/10.1016/j.apenergy.2014.12.089).
- [4] E. Ferrero, S. Alessandrini, A. Balanzino, Impact of the electric vehicles on the air pollution from a highway, *Appl. Energy* 169 (2016) 450–459, doi:[10.1016/j.apenergy.2016.01.098](https://doi.org/10.1016/j.apenergy.2016.01.098).
- [5] E.A.M. Falcão, A.C.R. Teixeira, J.R. Sodré, Analysis of CO<sub>2</sub> emissions and techno-economic feasibility of an electric commercial vehicle, *Appl. Energy* 193 (2017) 297–307, doi:[10.1016/j.apenergy.2017.02.050](https://doi.org/10.1016/j.apenergy.2017.02.050).
- [6] P. Mock, Z. Yang, Driving electrification: A global comparison of fiscal incentive policy for electric vehicles, White Paper, The International Council on Clean Transportation, Washington, DC, USA, 2014 White Paper.
- [7] S. Loehmann, M. Landau, M. Koerber, A. Butz, Heartbeat: Experience the pulse of an electric vehicle, in: Proc. 6th Int. Conf. Automot. User Interfaces Interact. Veh. Appl., Seattle, WA, USA, Association for Computing Machinery, 2014, pp. 1–10, doi:[10.1145/2667317.2667331](https://doi.org/10.1145/2667317.2667331).
- [8] International energy outlook 2019, U.S. Energy Information Administration, Office of Energy Analysis, U.S. Department of Energy, Washington, DC, USA, 2019.
- [9] SAE electric vehicle and plug in hybrid electric vehicle conductive charge coupler, Standard J1772\_201710, SAE International, Warrendale, PA, USA, 2017, doi:10.4271/J1772\_201710.
- [10] M. Yilmaz, P.T. Krein, Review of battery charger topologies, charging power levels, and infrastructure for plug-in electric and hybrid vehicles, *IEEE Trans. Power Electron.* 28 (5) (2013) 2151–2169, doi:[10.1109/TPEL.2012.2212917](https://doi.org/10.1109/TPEL.2012.2212917).
- [11] H.S. Das, M.M. Rahman, S. Li, C.W. Tan, Electric vehicles standards, charging infrastructure, and impact on grid integration: A technological review, *Renewable Sustainable Energy Rev* 120 (2020) 109618, doi:[10.1016/j.rser.2019.109618](https://doi.org/10.1016/j.rser.2019.109618).
- [12] IEEE standard technical specifications of a DC quick charger for use with electric vehicles, IEEE Standard 2030.1.1–2015, IEEE Vehicular Technology Society, New York, NY, USA, 2016, doi:10.1109/IEEESTD.2016.7400449.
- [13] M. Knez, G.K. Zevnik, M. Obrecht, A review of available chargers for electric vehicles: United States of America, European Union, and Asia, *Renewable Sustainable Energy Rev* 109 (2019) 284–293, doi:[10.1016/j.rser.2019.04.013](https://doi.org/10.1016/j.rser.2019.04.013).
- [14] A. Meintz, J. Zhang, R. Vijayagopal, C. Kreutzer, S. Ahmed, I. Bloom, A. Burnham, R.B. Carlson, F. Dias, E.J. Dufek, J. Francfort, K. Hardy, A.N. Jansen, M. Keyser, A. Markel, C. Michelbacher, M. Mohanpurkar, A. Pesaran, D. Scoffield, M. Shirk, T. Stephens, T. Tanim, Enabling fast charging – Vehicle considerations, *J. Power Sources* 367 (2017) 216–227, doi:[10.1016/j.jpowsour.2017.07.093](https://doi.org/10.1016/j.jpowsour.2017.07.093).
- [15] J. Dixon, P. Bach, K. Bell, C. Træholt, On the ease of being green: An investigation of the inconvenience of electric vehicle charging, *Appl. Energy* 258 (2020) 114090, doi:[10.1016/j.apenergy.2019.114090](https://doi.org/10.1016/j.apenergy.2019.114090).
- [16] N.S. Pearre, W. Kempton, R.L. Guensler, V.V. Elango, Electric vehicles: How much range is required for a day's driving? *Transp. Res. Part C Emerging Technol.* 19 (6) (2011) 1171–1184, doi:[10.1016/j.trc.2010.12.010](https://doi.org/10.1016/j.trc.2010.12.010).
- [17] I. Mudawar, Assessment of high-heat-flux thermal management schemes, *IEEE Trans. Compon. Packag. Technol.* 24 (2) (2001) 122–141, doi:[10.1109/6144.926375](https://doi.org/10.1109/6144.926375).
- [18] A.E. Bergles, W.M. Rohsenow, The determination of forced-convection surface-boiling heat transfer, *J. Heat Transfer* 86 (3) (1964) 365–372, doi:[10.1115/1.3688697](https://doi.org/10.1115/1.3688697).
- [19] J.R.S. Thom, W.M. Walker, T.A. Fallon, G.F.S. Reising, Boiling in sub-cooled water during flow up heated tubes or annuli, *Proc. Inst. Mech. Eng.* 180 (3C) (1965) 226–246, doi:[10.1243/PIME\\_CONF\\_1965\\_180\\_117\\_02](https://doi.org/10.1243/PIME_CONF_1965_180_117_02).
- [20] R.W. Murphy, A.E. Bergles, Subcooled flow boiling of fluorocarbons, Report no. DSR 71903-72, Heat Transfer Laboratory, Department of Mechanical Engineering, Massachusetts Institute of Technology, Cambridge, MA, USA, 1971.
- [21] J. Shaw, Subcooled boiling heat transfer to liquids under conditions of forced convection, Ph.D. Thesis, Chemical Engineering, University of Surrey, Guildford, Surrey, UK, 1972 PhD Thesis.
- [22] H. Müller-Steinhagen, A.P. Watkinson, N. Epstein, Subcooled-boiling and convective heat transfer to heptane flowing inside an annulus and past a coiled wire: Part I—Experimental results, *J. Heat Transfer* 108 (4) (1986) 922–927, doi:[10.1115/1.3247035](https://doi.org/10.1115/1.3247035).
- [23] A. Hasan, R.P. Roy, S.P. Kalra, Experiments on subcooled flow boiling heat transfer in a vertical annular channel, *Int. J. Heat Mass Transfer* 33 (10) (1990) 2285–2293, doi:[10.1016/0017-9310\(90\)90127-G](https://doi.org/10.1016/0017-9310(90)90127-G).
- [24] N. Kattan, J.R. Thome, D. Favrat, Convective boiling and two-phase flow patterns in an annulus, in: Atti Del X Congresso Nazionale Sulla Transmisione Del Calore, Università degli Studi di Genova, Genoa, Italy, 1992, pp. 309–320.
- [25] R.E. Lundberg, W.C. Reynolds, W.M. Kays, Heat transfer with laminar flow in concentric annuli with constant and variable wall temperature with heat flux, NASA Technical Note D-1972, Washington, DC, USA, 1963.
- [26] W.M. Rohsenow, J.P. Hartnett, Y.I. Cho, *Handbook of Heat Transfer*, 3rd ed., McGraw-Hill Inc., New York, NY, USA, 1998.
- [27] V.S. Devahdhanush, S. Lee, I. Mudawar, Experimental investigation of sub-cooled flow boiling in annuli with reference to thermal management of ultra-fast electric vehicle charging cables, *Int. J. Heat Mass Transfer* 172 (2021) 121176 in press, doi:[10.1016/j.ijheatmasstransfer.2021.121176](https://doi.org/10.1016/j.ijheatmasstransfer.2021.121176).
- [28] F.D. Moles, J.F.G. Shaw, Boiling heat transfer to sub-cooled liquids under conditions of forced convection, *Trans. Inst. Chem. Eng.* 50 (1) (1972) 76–84.
- [29] S.M. Kim, I. Mudawar, Review of databases and predictive methods for pressure drop in adiabatic, condensing and boiling mini/micro-channel flows, *Int. J. Heat Mass Transfer* 77 (2014) 74–97, doi:[10.1016/j.ijheatmasstransfer.2014.04.035](https://doi.org/10.1016/j.ijheatmasstransfer.2014.04.035).
- [30] K.E. Gungor, R.H.S. Winterton, A general correlation for flow boiling in tubes and annuli, *Int. J. Heat Mass Transfer* 29 (3) (1986) 351–358, doi:[10.1016/0017-9310\(86\)90205-X](https://doi.org/10.1016/0017-9310(86)90205-X).
- [31] Z. Liu, R.H.S. Winterton, A general correlation for saturated and subcooled flow boiling in tubes and annuli, based on a nucleate pool boiling equation, *Int. J. Heat Mass Transfer* 34 (11) (1991) 2759–2766, doi:[10.1016/0017-9310\(91\)90234-6](https://doi.org/10.1016/0017-9310(91)90234-6).
- [32] C.R. Kharangate, I. Mudawar, Review of computational studies on boiling and condensation, *Int. J. Heat Mass Transfer* 108 (2017) 1164–1196, doi:[10.1016/j.ijheatmasstransfer.2016.12.065](https://doi.org/10.1016/j.ijheatmasstransfer.2016.12.065).
- [33] V.S. Devahdhanush, Y. Lei, Z. Chen, I. Mudawar, Assessing advantages and disadvantages of macro- and micro-channel flow boiling for high-heat-flux thermal management using computational and theoretical/empirical methods, *Int. J. Heat Mass Transfer* 169 (2021) 120787, doi:[10.1016/j.ijheatmasstransfer.2020.120787](https://doi.org/10.1016/j.ijheatmasstransfer.2020.120787).
- [34] S.M. Kim, I. Mudawar, Consolidated method to predicting pressure drop and heat transfer coefficient for both subcooled and saturated flow boiling in micro-channel heat sinks, *Int. J. Heat Mass Transfer* 55 (13–14) (2012) 3720–3731, doi:[10.1016/j.ijheatmasstransfer.2012.02.061](https://doi.org/10.1016/j.ijheatmasstransfer.2012.02.061).
- [35] T.L. Bergman, A.S. Lavine, F.P. Incropera, D.P. Dewitt, *Fundamentals of Heat and Mass Transfer*, 8th ed., John Wiley & Sons, Inc., New York, NY, USA, 2017.
- [36] R.W. Hanks, The laminar-turbulent transition for flow in pipes, concentric annuli, and parallel plates, *AIChE J* 9 (1) (1963) 45–48, doi:[10.1002/aic.690090110](https://doi.org/10.1002/aic.690090110).
- [37] J.G. Collier, J.R. Thome, *Convective Boiling and Condensation*, 3rd ed., Clarendon Press, Oxford, UK, 1994.
- [38] G.E. Geiger, Sudden contraction losses in single and two-phase flow, Ph.D. Thesis, University of Pittsburgh, PA, USA, 1964 PhD Thesis.
- [39] J. Schmidt, L. Friedel, Two-phase pressure drop across sudden contractions in duct areas, *Int. J. Multiphase Flow* 23 (2) (1997) 283–299, doi:[10.1016/s0301-9322\(96\)00056-0](https://doi.org/10.1016/s0301-9322(96)00056-0).
- [40] F.F. Abdelall, G. Hahn, S.M. Ghiaasiaan, S.I. Abdel-Khalik, S.S. Jeter, M. Yoda, D.L. Sadowski, Pressure drop caused by abrupt flow area changes in small channels, *Exp. Therm. Fluid Sci.* 29 (4) (2005) 425–434, doi:[10.1016/j.expthermflusci.2004.05.001](https://doi.org/10.1016/j.expthermflusci.2004.05.001).
- [41] J. Liu, *Flow of a Bingham fluid in the entrance region of an annular tube*, M.S. Thesis, University of Wisconsin-Milwaukee, WI, USA, 1974 MS Thesis.
- [42] R.K. Shah, A.L. London, *Laminar Flow Forced Convection in Ducts: A Source Book for Compact Heat Exchanger Analytical Data*, Elsevier, New York, NY, USA, 1978, doi:[10.1016/C2013-0-06152-X](https://doi.org/10.1016/C2013-0-06152-X).
- [43] R.K. Shah, A correlation for laminar hydrodynamic entry length solutions for circular and noncircular ducts, *J. Fluids Eng.* 100 (2) (1978) 177–179, doi:[10.1115/1.3448626](https://doi.org/10.1115/1.3448626).
- [44] O.C. Jones, J.C.M. Leung, An improvement in the calculation of turbulent friction in smooth concentric annuli, *J. Fluids Eng.* 103 (4) (1981) 615–623, doi:[10.1115/1.3241781](https://doi.org/10.1115/1.3241781).
- [45] M.S. Bhatti, R.K. Shah, *Turbulent and transition flow convective heat transfer in ducts*, in: S. Kakac, R.K. Shah, W. Aung (Eds.), *Handbook of Single-Phase Convective Heat Transfer*, Wiley-Interscience, New York, NY, USA, 1987.
- [46] S.M. Ghiaasiaan, *Convective Heat and Mass Transfer*, 2nd ed., CRC Press, Boca Raton, FL, USA, 2018.
- [47] R.M. Olson, E.M. Sparrow, Measurements of turbulent flow development in tubes and annuli with square or rounded entrances, *AIChE J* 9 (6) (1963) 766–770, doi:[10.1002/aic.690090612](https://doi.org/10.1002/aic.690090612).
- [48] B. Shome, Entrance length and friction factor correlations for turbulent flow in concentric annuli, *Int. J. Fluid Mech. Res.* 45 (3) (2018) 255–262, doi:[10.1615/InterFluidMechRes.2018020326](https://doi.org/10.1615/InterFluidMechRes.2018020326).

- [49] W. Zhi-qing, Study on correction coefficients of laminar and turbulent entrance region effect in round pipe, *Appl. Math. Mech.* 3 (1982) 433–446, doi:[10.1007/BF01897224](https://doi.org/10.1007/BF01897224).
- [50] T. Sato, H. Matsumura, On the conditions of incipient subcooled-boiling with forced convection, *Bull. JSME* 7 (26) (1964) 392–398, doi:[10.1299/jsme1958.7.392](https://doi.org/10.1299/jsme1958.7.392).
- [51] E. Hahne, K. Spindler, H. Skok, A new pressure drop correlation for subcooled flow boiling of refrigerants, *Int. J. Heat Mass Transfer* 36 (17) (1993) 4267–4274, doi:[10.1016/0017-9310\(93\)90089-O](https://doi.org/10.1016/0017-9310(93)90089-O).
- [52] D.R.H. Beattie, P.B. Whalley, A simple two-phase frictional pressure drop calculation method, *Int. J. Multiphase Flow* 8 (1) (1982) 83–87, doi:[10.1016/0301-9322\(82\)90009-X](https://doi.org/10.1016/0301-9322(82)90009-X).
- [53] S.M. Kim, I. Mudawar, Universal approach to predicting two-phase frictional pressure drop for adiabatic and condensing mini/micro-channel flows, *Int. J. Heat Mass Transfer* 55 (11–12) (2012) 3246–3261, doi:[10.1016/j.ijheatmasstransfer.2012.02.047](https://doi.org/10.1016/j.ijheatmasstransfer.2012.02.047).
- [54] S.M. Kim, I. Mudawar, Universal approach to predicting two-phase frictional pressure drop for mini/micro-channel saturated flow boiling, *Int. J. Heat Mass Transfer* 58 (1–2) (2013) 718–734, doi:[10.1016/j.ijheatmasstransfer.2012.11.045](https://doi.org/10.1016/j.ijheatmasstransfer.2012.11.045).
- [55] S. Kakac, Y. Yener, *Convective Heat Transfer*, 2nd ed., CRC Press, Boca Raton, FL, USA, 1995.
- [56] S. Kakac, O. Yucel, Laminar flow heat transfer in an annulus with simultaneous development of velocity and temperature fields, Technical and Scientific Council of Turkey, TUBITAK, ISITEK Report No. 19, Antara, Turkey, 1974.
- [57] H.S. Heaton, W.C. Reynolds, W.M. Kays, Heat transfer in annular passages. Simultaneous development of velocity and temperature fields in laminar flow, *Int. J. Heat Mass Transfer* 7 (7) (1964) 763–781, doi:[10.1016/0017-9310\(64\)90006-7](https://doi.org/10.1016/0017-9310(64)90006-7).
- [58] R.E. Lundberg, P.A. McCuen, W.C. Reynolds, Heat transfer in annular passages. Hydrodynamically developed laminar flow with arbitrarily prescribed wall temperatures or heat fluxes, *Int. J. Heat Mass Transfer* 6 (6) (1963) 495–529, doi:[10.1016/0017-9310\(63\)90124-8](https://doi.org/10.1016/0017-9310(63)90124-8).
- [59] P.M. Worsøe-Schmidt, Heat transfer in the thermal entrance region of circular tubes and annular passages with fully developed laminar flow, *Int. J. Heat Mass Transfer* 10 (4) (1967) 541–551, doi:[10.1016/0017-9310\(67\)90173-1](https://doi.org/10.1016/0017-9310(67)90173-1).
- [60] A. Quaraby, Some measurements of turbulent heat transfer in the thermal entrance region of concentric annuli, *Int. J. Heat Mass Transfer* 10 (3) (1967) 267–276, doi:[10.1016/0017-9310\(67\)90144-5](https://doi.org/10.1016/0017-9310(67)90144-5).
- [61] Y. Lee, Turbulent heat transfer from the core tube in thermal entrance regions of concentric annuli, *Int. J. Heat Mass Transfer* 11 (3) (1968) 509–522, doi:[10.1016/0017-9310\(68\)90093-8](https://doi.org/10.1016/0017-9310(68)90093-8).
- [62] Y. Lee, S.D. Park, Developing turbulent flow and heat transfer in concentric annuli, *Trans. Can. Soc. Mech. Eng.* 1 (1) (1972) 13–24, doi:[10.1139/tcsm-1972-0002](https://doi.org/10.1139/tcsm-1972-0002).
- [63] R.H. Notter, C.A. Sleicher, A solution to the turbulent Graetz problem-III Fully developed and entry region heat transfer rates, *Chem. Eng. Sci.* 27 (11) (1972) 2073–2093, doi:[10.1016/0009-2509\(72\)87065-9](https://doi.org/10.1016/0009-2509(72)87065-9).
- [64] M. Al-Arabi, Turbulent heat transfer in the entrance region of a tube, *Heat Transfer Eng.* 3 (3–4) (1982) 76–83, doi:[10.1080/01457638108939586](https://doi.org/10.1080/01457638108939586).
- [65] W.M. Kays, E.Y. Leung, Heat transfer in annular passages—hydrodynamically developed turbulent flow with arbitrarily prescribed heat flux, *Int. J. Heat Mass Transfer* 6 (7) (1963) 537–557, doi:[10.1016/0017-9310\(63\)90012-7](https://doi.org/10.1016/0017-9310(63)90012-7).
- [66] A. Roberts, H. Barrow, Turbulent heat transfer to air in the vicinity of the entry of an internally heated annulus, *Proc. Inst. Mech. Eng.* 182 (3H) (1967) 268–276, doi:[10.1243/pime\\_conf\\_1967\\_182\\_238\\_02](https://doi.org/10.1243/pime_conf_1967_182_238_02).
- [67] K.E. Gungor, R.H.S. Winterton, Simplified general correlation for saturated flow boiling and comparisons of correlations with data, *Chem. Eng. Res. Des.* 65 (2) (1987) 148–156.
- [68] S.M. Kim, I. Mudawar, Universal approach to predicting saturated flow boiling heat transfer in mini/micro-channels – Part II. Two-phase heat transfer coefficient, *Int. J. Heat Mass Transfer* 64 (2013) 1239–1256, doi:[10.1016/j.ijheatmasstransfer.2013.04.014](https://doi.org/10.1016/j.ijheatmasstransfer.2013.04.014).
- [69] M.M. Shah, Evaluation of general correlations for heat transfer during boiling of saturated liquids in tubes and annuli, *HVAC&R Res.* 12 (4) (2006) 1047–1063, doi:[10.1080/10789669.2006.10391450](https://doi.org/10.1080/10789669.2006.10391450).
- [70] M.M. Shah, Chart correlation for saturated boiling heat transfer: Equations and further study, *ASHRAE Trans.* 88 (1982) 185–196.
- [71] L.E. O'Neill, I. Park, C.R. Kharangate, V.S. Devahdhanush, V. Ganesan, I. Mudawar, Assessment of body force effects in flow condensation, part II: Criteria for negating influence of gravity, *Int. J. Heat Mass Transfer* 106 (2017) 313–328, doi:[10.1016/j.ijheatmasstransfer.2016.07.019](https://doi.org/10.1016/j.ijheatmasstransfer.2016.07.019).
- [72] Y.M. Lie, T.F. Lin, Subcooled flow boiling heat transfer and associated bubble characteristics of R-134a in a narrow annular duct, *Int. J. Heat Mass Transfer* 49 (13–14) (2006) 2077–2089, doi:[10.1016/j.ijheatmasstransfer.2005.11.032](https://doi.org/10.1016/j.ijheatmasstransfer.2005.11.032).
- [73] H. Zhang, I. Mudawar, M.M. Hasan, Experimental and theoretical study of orientation effects on flow boiling CHF, *Int. J. Heat Mass Transfer* 45 (22) (2002) 4463–4477, doi:[10.1016/S0017-9310\(02\)00152-7](https://doi.org/10.1016/S0017-9310(02)00152-7).
- [74] C. Konishi, I. Mudawar, Review of flow boiling and critical heat flux in microgravity, *Int. J. Heat Mass Transfer* 80 (2015) 469–493, doi:[10.1016/j.ijheatmasstransfer.2014.09.017](https://doi.org/10.1016/j.ijheatmasstransfer.2014.09.017).
- [75] S.M. Kim, I. Mudawar, Universal approach to predicting saturated flow boiling heat transfer in mini/micro-channels – Part I. Dryout incipience quality, *Int. J. Heat Mass Transfer* 64 (2013) 1226–1238, doi:[10.1016/j.ijheatmasstransfer.2013.04.016](https://doi.org/10.1016/j.ijheatmasstransfer.2013.04.016).
- [76] S.M. Kim, I. Mudawar, Theoretical model for annular flow condensation in rectangular micro-channels, *Int. J. Heat Mass Transfer* 55 (4) (2012) 958–970, doi:[10.1016/j.ijheatmasstransfer.2011.10.014](https://doi.org/10.1016/j.ijheatmasstransfer.2011.10.014).
- [77] H. Lee, C.R. Kharangate, N. Mascarenhas, I. Park, I. Mudawar, Experimental and computational investigation of vertical downflow condensation, *Int. J. Heat Mass Transfer* 85 (2015) 865–879, doi:[10.1016/j.ijheatmasstransfer.2015.02.037](https://doi.org/10.1016/j.ijheatmasstransfer.2015.02.037).